Unterschrift BetreuerIn

DIPLOMARBEIT

Generation of ion pulses in a fast pulsed EBIS supported by realistic ion trajectory simulations

ausgeführt am Institut für Angewandte Physik
der Technischen Universität Wien

unter der Anleitung von
Richard A. Wilhelm
Gabriel L. Szabo

durch

Alexander S. Grossek

[redacted]

December 12, 2022

Unterschrift StudentIn

Abstract

The time4ions group aims to conduct novel pump/probe experiments on particle systems, using ion pulses as the pump mechanism combined with a laser pulses as the probe mechanism. Such pump/probe experiments will be used to resolve the relaxation dynamics of collision cascades in materials induced by the ion pulse impact. Since such collision cascades occur on the sub-nanosecond timescale accurate measurements of the relaxation require ion pulses with below sub-nanosecond pulse widths. We generate ion pulses in two steps. In the first step, we utilize a femtosecond laser directed onto a cathode to produce pulsed photo-electrons by photo-emission in a electron beam ion source (EBIS). The EBIS is placed in a vacuum chamber filled with low pressure gaseous argon or nitrogen. In the second step, the pulsed photo-electrons interact with the gas, among other processes, via pulsed electron impact ionisation (EII). If EII occurs in a volume in the EBIS surrounded by a potential slope, we get pulsed ions with pulse widths dependent on the potentials set to the EBIS electrode assembly. The pulsed electrons and ions time of flight (TOF) is measured, and from their TOF distribution we evaluate the pulse width.

Currently the main focus of the experiment lies in the process of ion pulse generation. The EBIS we use covers nearly the full solid angle around the cathode. The only solid angle through which the cathode is accessible is given by the exit opening of EBIS. A few complications arise in this setup. First we have to direct the femtosecond laser onto the cathode through the exit of the EBIS. This requires us to place a optical mirror close the beam axis of the EBIS, blocking a part of our ion/electron beam. We tested the EBIS in two distinct assembly configurations called the half-EBIS and full-EBIS operation. The advantage of the half-EBIS operation is a bigger opening solid angle for accessing the cathode, however we lose the ability to prevent EII outside the EBIS. The ions produced outside the EBIS have no temporal structure which distorts our pulse width during TOF measurements. In the full-EBIS operation we can prevent most electrons leaking out of the EBIS, however this comes at a cost of a reduced opening solid angle which forces us to place the optical mirror closer to the beam axis, cutting more of our particle beam.

We have been able to produce electron pulses with both EBIS setups at pulse widths in the mid 100 ps magnitude range, with the electron pulse width showing a weak dependency on the cathode potential. In the half-EBIS operation we were not able to create reproducible ion pulses. In full-EBIS operation a clear ion pulse is not yet visible, however the TOF spectra shows temporal structure in direct relation to the femtosecond laser repetition rate. Furthermore measurements of pulsed photo-electron emission currents from the cathode are shown to be relatively small to the detriment of ion pulse generation.

Kurzfassung

Die time4ions-Gruppe zielt darauf ab, neuartige pump/probe -Experimente an Teilchensystemen durchzuführen, hierbei werden Ionenpulse als 'pump'-mechanismus und Laserpulse als 'probe'-mechanismus kombiniert. Wir werden solche pump/probe -Experimente verwenden um die Relaxationsdynamik von Kollisionskaskaden in Materialien aufzulösen, die durch den Aufprall vom Ionenpuls auf das Material induziert werden. Da solche Kollisionskaskaden auf unter Nanosekunden-Zeitskalen stattfinden, erfordern genaue Messungen dieser Relaxation Ionenpulse mit Pulsbreiten unterhalb von Nanosekunden. Wir erzeugen Ionenpulse in zwei Schritten. Im ersten Schritt verwenden wir einen auf eine Kathode gerichteten Femtosekundenlaser, um gepulste Photoelektronen durch Photoemission in einer Elektronenstrahl-Ionenquelle (EBIS) zu erzeugen. Die EBIS wird in einer Vakuumkammer platziert, die mit gasförmigem Niederdruck-Argon oder -Stickstoff gefüllt wird. Im zweiten Schritt wechselwirken die gepulsten Photoelektronen mit dem Gas, unter anderem durch gepulste Elektronenstoßionisation (EII). Wenn EII innerhalb eines bestimmten Volumens in der EBIS auftritt, das von einer Potentialsteigung umgeben ist, erhalten wir gepulste Ionen mit Pulsbreiten, die von den an der EBIS-Elektrodenanordnung eingestellten Potentialen abhängen. Die gepulsten Elektronen- und Ionenflugzeiten (TOF) wird gemessen, und anhand ihrer TOF-Verteilung werten wir die Pulsbreite aus.

Derzeit liegt das Hauptaugenmerk des Experiments auf dem Prozess der Ionenpulserzeugung. Die von uns verwendete EBIS deckt nahezu den vollen Raumwinkel um die Kathode ab. Der einzige Raumwinkel, durch den die Kathode zugänglich ist, ist durch die Austrittsöffnung der EBIS gegeben. Bei diesem Setup treten einige Komplikationen auf. Zuerst müssen wir den Femtosekundenlaser durch die Austrittsöffnung der EBIS auf die Kathode richten. Dazu müssen wir einen optischen Spiegel nahe der Strahlachse der EBIS platzieren, der einen Teil unseres Ionen-/Elektronenstrahls blockieren kann. Wir haben die EBIS in zwei unterschiedlichen Montagekonfigurationen getestet, die als Halb-EBIS- und Voll-EBIS-Betrieb bezeichnet werden. Der Vorteil des Halb-EBIS-Betriebs ist ein größerer Öffnungsraumwinkel für den Zugang zur Kathode, jedoch verlieren wir die Fähigkeit, EII außerhalb des EBIS zu verhindern. Die außerhalb der EBIS produzierten Ionen haben keine zeitliche Struktur und verzerren somit unsere Pulsbreite bei TOF-Messungen. Im Voll-EBIS-Betrieb können wir verhindern, dass die Elektronen aus der EBIS austreten, dies geht jedoch auf Kosten eines reduzierten Öffnungsraumwinkel, der

uns dazu zwingt, den optischen Spiegel näher an der Strahlachse zu platzieren und somit mehr von unserem Teilchenstrahl blockieren kann.

Wir konnten mit beiden EBIS-Aufbauten Elektronenpulse mit Pulsbreiten im mittleren 100-ps-Größenbereich erzeugen, wobei die Elektronenpulsbreite eine schwache Abhängigkeit vom Kathodenpotential zeigt. Im Halb-EBIS-Betrieb konnten wir keine reproduzierbaren Ionenpulse erzeugen. Im Full-EBIS-Betrieb ist noch kein deutlicher Ionenpuls sichtbar, jedoch zeigt das TOF-Spektrum eine zeitliche Struktur in direktem Zusammenhang mit der Femtolaser-Wiederholungsrate. Darüber hinaus haben Messungen vom gepulsten Photoelektronenstrom gezeigt, dass diese Ströme verhältnismäßig niedrig sind um ein genügende Anzahl von Ionen zu erzeugen.

Contents

1. Introduction

New and improved materials are a driver for human prosperity in modern society. As such there is an ongoing economic demand for improved performance of materials. In the most general terms materials depending on their purpose can be improved in many different aspects such as durability, conductivity, surface roughness, hardness, structure, etc. Many economic sectors rely on materials researcher to provide these advancements. The physical phenomena that deliver the desired effects of these materials occur on the nano-scale. As such a considerable amount of investments have been put into the research of this field [1].

The main focus here is the functionalization of materials on the nano-scale, where one of the tools for functionalization is by ion irradiation. This enables the manipulation of material properties via effects of ion implantation, and nanostructuring[2–6]. In semiconductors ion implantation is used to produce materials with different band gaps [7]. These materials enable the developement of transistors for high power electronics to nano transistors for modern integrated circuits. Electronic properties of low dimensional materials may also be modified via nanostructuring by ion bombardment [8], however the utilizations for nanostructuring go well beyond that. In order to improve ion bombardment as a more versatile tool for material functionalization it is necessary to gain a better understanding of dynamics leading to nanostructuring. For this purpose we want to investigate the collisional cascades and the subsequent relaxation that occur within a material upon ion impact.

The time4ions project aims to design and operate an experiment in order to explore the time regime at which collisional cascades occur on thin film materials impacted by an ion. Collisional cascades are a series of collisions between the atoms in a material. This series is set off by the initial impact by the ion. Such interactions fall into the category of non-equilibrium relaxation dynamics. We plan to gain insights into this phenomena by utilizing the concepts of pump/probe experiments in a novel way. The fundamental concept behind pump/probe experiments is the excitation of a system via a "pump" signal followed by a subsequent time delayed "probe" signal to determine the current state of the system. Once the system has been pumped, it enters an unstable state and starts to relax back into a stable state by dissipating the energy of the pump. Varying the time delay between pump and probe signals we can record the progression

through-out the relaxation process. While most pump-probe experiments make use of laser pulses for both the pump and the probe as it was developed by Ahmed H. Zewail [9], we want to combine laser probe pulses with ion pump pulses. The concept of applying the pump-probe technique utilizing ions as pump for the target is a promising and novel technique for the study of time-resolved ion-solid interactions. Since the processes of these collisional cascades in thin film materials are hypothesised to take place in the sub-nanosecond regime, ion pulses with a pulse width at-least a magnitude below sub-nanoseconds are needed for accurate measurements.

There exist multiple possibilities to produce sub-nanosecond pulsed ions. Some of the methods utilize an ultra fast pulsed laser source, with pulse widths in the femtosecond regime. One method (built by the group of M. Schleberger of the University Duisburg) utilizes an ultra short pulsed laser source to directly ionize the atoms in a gas jet (see Fig. 1.1). The energy density of the ultra short laser pulse is high enough to directly remove an electron from the electronic structure of the atoms in the gas jet. In order to create an ion pulse from this method the intersection point between laser beam and gas jet is surrounded by electrode plates which separate the ions via a potential gradient

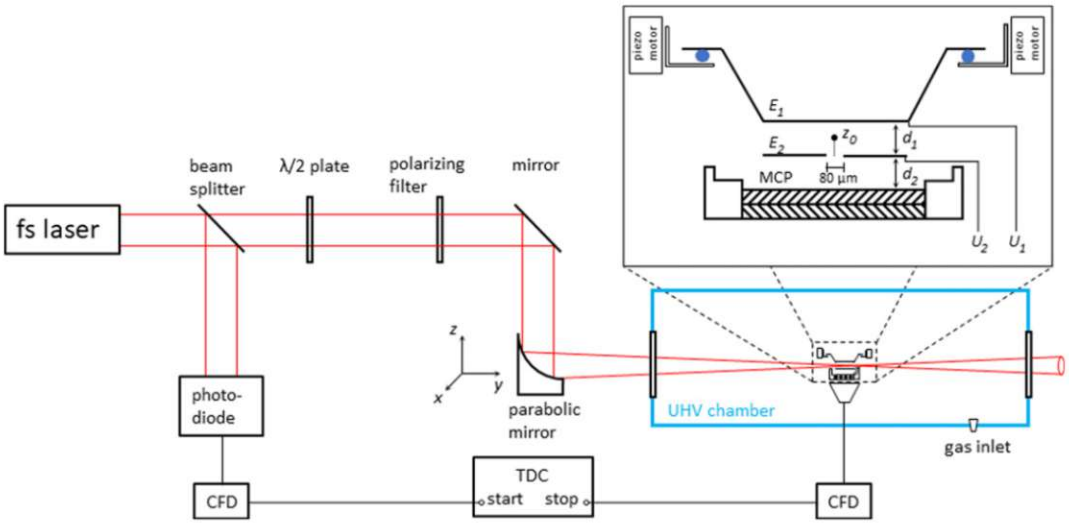

Figure 1.1.: Schematic of the production of pulsed ions via direct photo ionization, taken from [10]. A pulsed femto-second laser is guided into a ultra high vacuum chamber (UHV). A parabolic mirror places the focal point of the laser in the UHV chamber in the center of a pair of electrode plates. The energy density at the focal point is high enough to directly ionize the gas. The ions are then accelerated by the electrodes on to a particle detector.

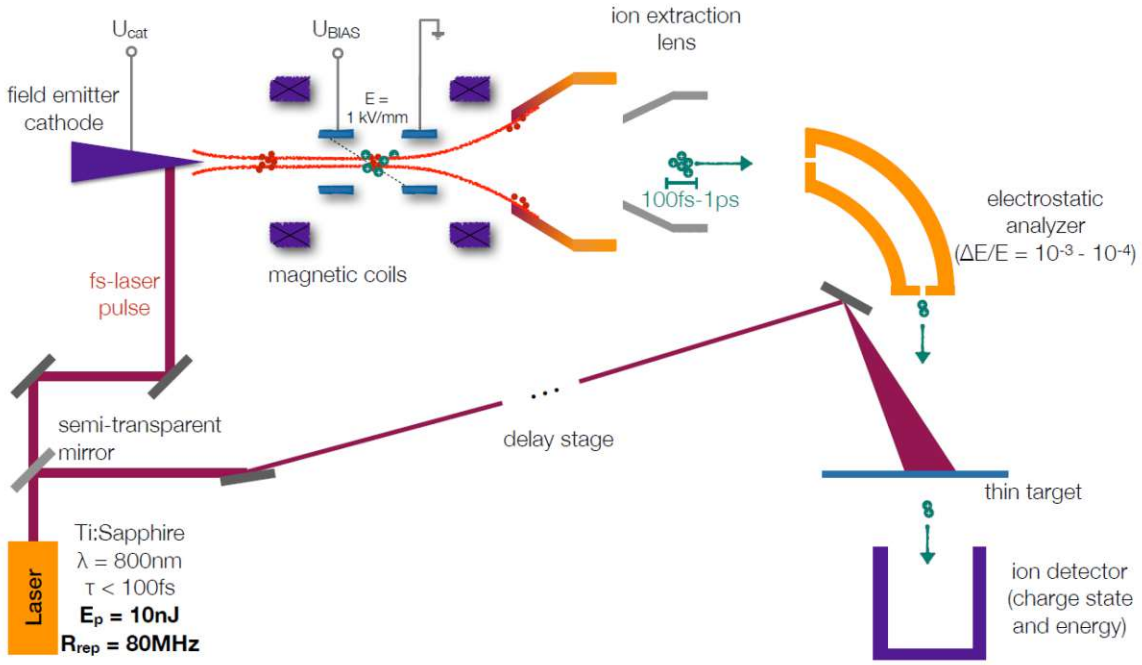

Figure 1.2.: Schematic of the production of pulsed ions via indirect ionization, taken from [12]. A pulsed femto-second laser is guided into a UHV chamber and directed into an electron beam ion source (EBIS). The laser pulse extracts electrons from a cathode. The emitted electrons ionise the gas. The ions are subsequently accelerated in the EBIS.

from the gas jet[10, 11]. In Figure 1.2 an other method (built in our lab at the TU Wien) to produce sub-nano second ion pulses which utilizes an indirect ionization process is shown. In this method the ultra short laser pulse is directed onto a cathode, which emits an electron pulse induced by photo-emission. This electron pulse interacts with the gas in a vacuum chamber which leads to ionization of gas atoms via electron impact ionisation (EII). In this process the impinging electron knocks out a bound electron from the atom. The whole process takes place within an electron beam ion source (EBIS) consisting of rotational symmetric electrodes. The electron pulse should ideally create a small localized pocket of ions. By applying a potential gradient around the ion pocket within the EBIS we can extract the ions as a pulse. In our group and as part of this thesis we currently employ the indirect method of ionization in the experiment, because it avoids the use of an expensive and demanding laser system.

The current stage of the experiment is still focused on the creation and optimization of the ion pulses. For this purpose we have operated the experiment with two distinct

variations of the EBIS, once in half-EBIS operation and once in full-EBIS operation. This needed to be done because we currently do not direct our laser onto the cathode from the side as shown in Fig. 1.2, instead we enter the EBIS with the laser through the EBIS beam exit point. We direct our laser through the entire EBIS onto the cathode with a mirror place closely to the beam axis. We are confronted with varying complications depending on which EBIS operation type we use. The half-EBIS operation is missing the last three electrodes of the full-EBIS, which are used to focus the ion beam and filter electrons (more details in Sec. 3.2). The main advantage of the half-EBIS operation by removing these electrodes is that the cathode has wider acceptance angle for the ultra fast laser through the EBIS. As such the mirror which reflects the laser onto the cathode may be placed further away from the beam axis so it does not block any ions exiting the EBIS. Its main disadvantage is that we cannot filter the electrons which may result in ionizations occurring outside the EBIS. Ions created outside the EBIS cannot be used as a pulse. The described advantages and disadvantages of the half-EBIS operation are inversed for the full-EBIS operation. By measuring the time of flight (TOF) of the electrons and ions we can detect a pulse and determine their pulse width. We have managed to produce pulsed electrons with both setups. The half-EBIS operation and the full-EBIS operation being able to produce clean electron pulses at around 400 picosecond pulse widths. Ion pulse generation has proven to be more difficult. No clear ion pulses have been detected with either setup, however the full-EBIS operation did result in some non-random structures. As of today only thermal ions with no temporal structure have been measured with the half-EBIS operation. With the full-EBIS operation we were able to measure ion spectra with a temporal structure, indicating a clear relation to the periodicity of the femtosecond laser.

In parallel to conducting the experiment I also conducted simulations of ion and electron trajectories with the simulation software Simion and compare the simulated spectra to experimentally measured spectra. The simulation is designed to resemble the conditions in which the experiment is currently run as close as possible. I simulated the full EBIS configuration from electron creation to ion creation via virtual electron impact ionization (EII) with variable potentials of the EBIS electrodes and accurate magnetic fields. Since argon ions are the main ion species used in the experiment, I implement an analytic approximation of the argon EII cross section in the simulation. Mean free path lengths λ (pressure dependencies) along with other particle collision types such as elastic collisions and collisions resulting in excitation are not included in the simulation. Their inclusion in the simulation is assumed to mostly only influence the absolute number of ions generated which can be accounted for in the interpretation of the simulation results. Since these excluded interactions would most likely also have an effect in beam pulse broadening, the results of the simulation should to be regarded are idealistic and not realistically achievable. Previous works in which simulations have been conducted,

include extensive energy filtering evaluation schemes of particles to determine their pulse width. Since energy filtering is not part of the experiment yet, it is also not considered for the evaluation of the simulations in this thesis. The simulation results show electron pulses of around 50 picoseconds and ion pulses in the nanosecond region.

2. Working principles

2.1. Ionization processes and energies

The ionization of a atom or molecule means increasing or decreasing its charge state. This is done by by controlling the amount of electrons occupying states in their electronic structure. There are multiple methods of ionizing a particle. For our experiment two methods come into consideration. The first method being photo ionization and the second method being electron impact ionization.

In photo ionization a photon with energy $\hbar\omega$ is directed onto a particle, in our case this is an atom. If the energy of the photon is higher than the binding potential of an electron with the atomic nucleus, then there exists a probability that the electron will absorb the photons energy which enables the electron to escape the atom.

In electron impact ionization a high energy electron with energy $\frac{m_e v^2}{2}$ is directed onto an atom. In this scenario there exists a non zero probability that the free electron collides with an electron of the atom. If a collision takes place the free electron transfers kinetic energy to the bound electron. Similar to photo ionization, if the transferred energy is higher than the threshold ionization energy the bound electron may escape the atom leading to an ionized atom.

All elements have varying threshold ionization energies (see Fig. 2.1). The outer most electrons called the valence electrons occupy the most weakly bound electronic states of the atom. The threshold ionization energy is determined by these valence states. The first ionization energy for atomic hydrogen is 13.6 eV and 15.76 eV for argon. If the energy of the ionizing particle (photon, electron) is below this threshold, ionization cannot occur. However, in this case other processes may take place.

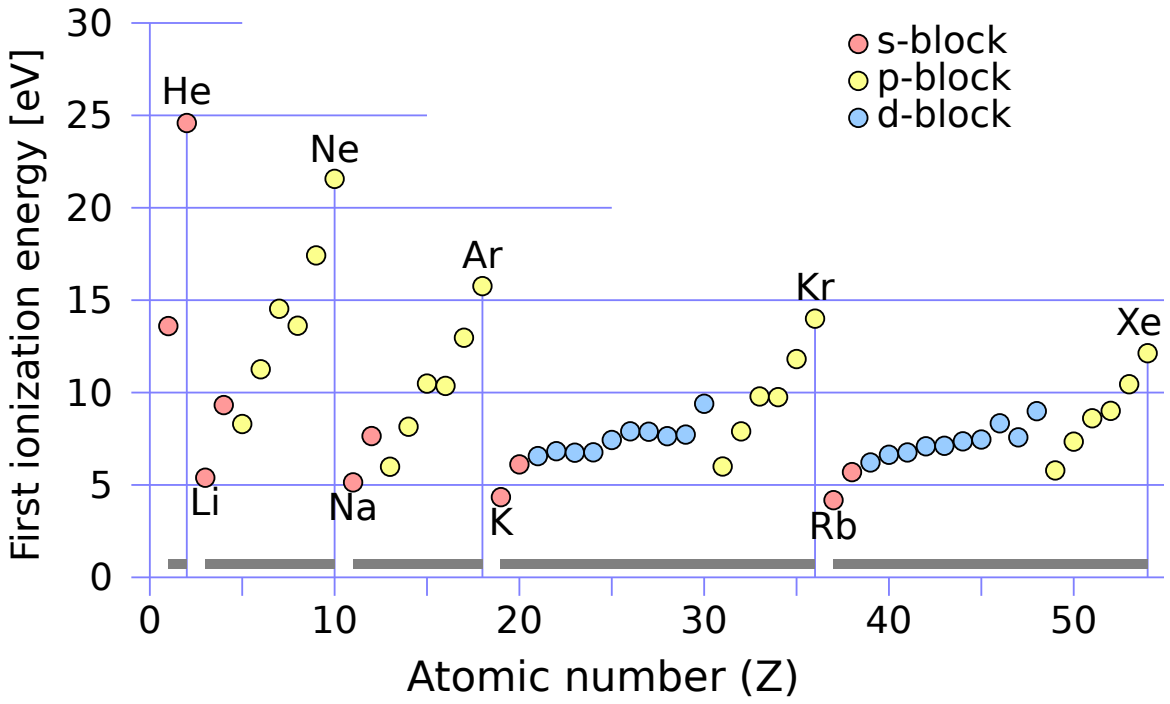

Figure 2.1.: The diagram shows the first ionization energies plotted over the atomic number of elements till Z = 54. The first ionization energy gradually trends down for which period in the periodic system. This first ionization energy is determined by the valence electrons of every element since these electrons occupy the most weakly bound states in the electronic structure. The color scheme indicates the electronic sub-shell the valence electrons inhabit. Argon has the fourth highest first ionization energy [13]

2.2. In search for analytical cross sections

Cross section is a rather broad term in physics. In general the term is used to describe the conditional probability of physical events, as in given the occurrence of physical event A what is the probability of physical event B. In our case physical event A is a collision between particles and the cross section is the probability indicator of physical event B occurring. Here we shall consider a collision between an electron and an atom. A plethora of physical phenomena may take place upon such a collision, which among other events may result in a fully elastic collision, in an excitation of an electron of the atom, or the ionization of the atom. All of these events have a non-zero probability of occurring given by their individual cross sections. As mentioned previously, the focus among ionization processes of this thesis lies in electron impact ionisation (EII), as such

the discussion of cross sections will also mostly be limited to the cross sections of EII. Specifically the EII cross section of argon is discussed, as argon is used as the main ion species in our experiment.

In the past century a considerable amount of experimental work has been conducted in an effort to ever more accurately determine cross sections in inelastic collisions. Researchers have gone as far as dissecting ionization cross sections for individual electronic shells of an atom. As a result of this work today we have a large repertoire of cross section data that we can draw from (argon: [14–19]), which has been useful in refining theoretical models used to calculate cross sections. Bretagne et al. (1986) derives the theoretical calculation of the differential cross sections in inelastic collisions for high energy charged particles with an atom with time-dependent perturbation theory combined with the first Born approximation [20]. This approach describes differential cross section at relativistic energies. This includes a form factor that usually includes a few unknown variables which make precise calculations difficult. Therefore, the relativistic form factor is instead approximated by the non-relativistic general oscillator strength, where the general oscillator strength basically gives the probability of the absorption or emission of a photon by the electronic structure of an atom. This approximation is a crucial step in the calculation since it relates high energy electron collisions to photon absorption processes, making use of the particle-wave duality. The equation is extended to the low energy collision domain by a multiplication with a empirical low-energy modifier factor. Bretagne et al. arrive to the following equation, for the total ionisation cross section.

$$\sigma_j(E) = B_j(E) \int_{I_j}^{\frac{E+I_j}{2}} S_j(E,T)\, dT \tag{1}$$

B_j is the empirical low-energy modifier factor, I_j is the ionisation energy, S_j is the differential ionisation cross section in E and T, where E represents in incident energy and T represents the transferred energy. The j-index signifies the electronic shell from which the previously bound electron is ejected. The ionisation energies for the K, L, M shells in argon are 3205 eV, 245 eV, and 15.76 eV respectively. The integral delivers very accurate results, however its explicit calculation is tedious since the differential ionisation cross section S_j is a complicated expression which includes an expression of the photo ionisation cross section of the considered atom species, leading to the point where we are describing cross sections with cross sections. 14 years before Bretagne et al., Peterson and Allen (1972) attempted the same calculation with a more practical approach. Peterson and Allen start their formulation of argon EII cross section via the Born approximation and use it to build a semiempirical method to reproduce the experimental data. Peterson and Allen derive curves for the differential ionization cross section, which they notice are well fitted by the Breit-Wigner function which fortunately

has a compact expression [21].

Peterson and Allen present a simple fit formula for argon based on Breit-Wigner function for the differential ionization cross section from the M-shell,

$$\begin{aligned} S_M(E,T) &= \frac{13.2}{E}\ln\left(\frac{E-\frac{120}{E}}{I_M}\right)\frac{10.3^2}{[T-T_0(E)]^2+10.3^2} \quad \text{with} \\ T_0(E) &= 2-\frac{10^2}{E+10} \end{aligned} \tag{2}$$

and a slightly shifted integration for the total differential cross section,

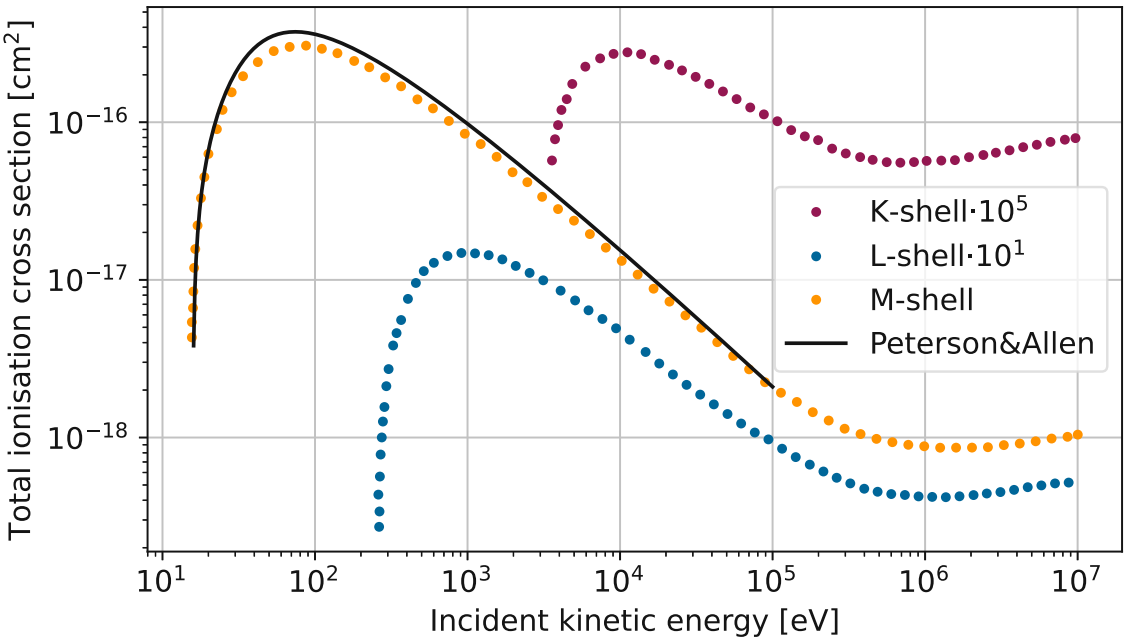

Figure 2.2.: Total ionisation cross section (TICS) for argon plotted over the incident kinetic energy in EII derived by Bretagne et al. [20] with Eq. 1. The three dotted curves show the TICS from each electronic shell. The inner K- and L-shells have significantly lower TICS than the valence M-shell. Their TICS have been scaled up by few magnitudes so they may be plotted in the same cross section region. Bretagne et al calculation fits the experimental TICS data very well. Peterson and Allen [21] TICS with Eq. 3 for the M-shell is overlaid in black. Peterson and Allen TICS slightly over estimates the TICS, however the calculation is much more simpler than Bretagne et al. and is used as a good approximation.

$$\sigma_j(E) = \int_0^{\frac{E-I_j}{2}} S_j(E,T)\, dT. \tag{3}$$

A similar equation is set up for L-shell contributions, while K-shell contributions are completely neglected, presumably due to their diminishing probability based on their relatively high ionization energy compared to M-, and L-shell. Although equations 2-3 deviate slightly more from experimental data compared to Bretagne et al (1986) (see Fig. 2.2) they are still very useful for quick practical applications since the Petersons and Allens differential ionization cross section can be easily integrated for the total ionization cross section. The calculation of equation 3, only considering M-shell contributions, leaves us with,

$$\sigma_M(E) = \frac{10.3 \times 13.2}{E} \ln\left(\frac{E^2 - 120}{I_M \cdot E}\right) \left[\tan^{-1}\left(\frac{T_0}{10.3}\right) - \tan^{-1}\left(\frac{2\,T_0 - E + I_M}{2 \times 10.3}\right)\right]. \tag{4}$$

2.3. Ion recoil momentum

In order to classify and simulate a particle beam it is very helpful to know the momenta distribution of the particle system before and especially after collisions. Knowledge of this property would allow the design of an efficient acceleration contraption in a beam source. Momenta distribution are calculated via the conservation of energy and momentum of the particles. In elastic collisions kinetic energy is conserved. In inelastic collisions one has to additionally consider kinetic energy losses to due internal particle excitations. Aside from the momentum distribution determining absolute velocities and velocity directions it also leads to particle positional spreading, these effects have direct influence on the pulse width when generating a pulsed beam which needs to considered in the simulation. McConkey et al (1972) [22] have measured the angular distribution of thermal-energy argon ions ionized by EII. In their study they state the transfer of momentum to be most dramatic for light ion species. In all ion species they measured apart from molecular hydrogen H_2^+ and atomic Helium He^+, the angular distribution of ions is well represented by a $\cos^2(\alpha)$ function where $\alpha = \frac{\pi}{2} - \vartheta = 0$ coincides with the angle of maximum ion intensity. The maximum occurs at an angle close to $\vartheta = \frac{\pi}{2}$ from the incident electron beam direction. This angular distribution is stated to be independent of incident energies, which were varied up to 300 eV [22].

2.4. Lasers and mode locking

Light amplification by simulated emission of radiation (laser) is a system which generates coherent monochromatic light. The main components of such laser systems consists of a light pump, gain medium, and an optical cavity. Which wavelength of light the system emits is largely dependent on the gain medium. The gain medium consists of a material in which multiple electronic states of the same energy are excitable. A constant excitation of the states is achieved through a light pump. Once a majority of states are excited, a so called population inversion is achieved which enables the lasing process. Through effects of spontaneous emission by state de-excitation photons of a single wavelength corresponding to the specific state are emitted. The gain medium is furthermore encapsulated in an optical cavity. The most simplistic setup of an optical cavity are 2 mirrors placed at a distance equal to a whole number multiple of the light wavelength in question. In such a cavity the photons resonate and are passed through the gain medium multiple times, triggering the emission of additional photons via stimulated emission. One of the mirrors in the optical cavity has a reflection index of $R < 1$, allowing some of the photons to escape the cavity creating a light beam.

This principle may be taken a step further. By utilizing a laser as the pump for a gain medium which houses multiple state transitions corresponding to different wavelengths and a more sophisticated optical cavity, one can essentially produce a laser consisting of multiple wavelengths, which generally oscillate out of phase. By mode locking these wavelengths they are put in phase which translates to coordinated destructive and constructive interference that produces a laser pulse. This case is a direct analogue to a inverse Fourier transformation of a signal from the frequency domain to the time domain. A monochromatic laser can be represented by a delta dirac distribution in frequency space which Fourier transforms into a constant function in time space. This property is also given in the opposite case. A delta dirac distribution in time space, which would represent a pulse with infinitely short pulse width, transforms into a constant function in frequency space. A constant function over the whole frequency domain resembles an ideal mode locked laser in which all wavelengths of the spectrum are present. This ideal case is unachievable, however it can be approximated. A mode locked laser may hold a number modes within a limited wavelength interval $\lambda \in [\lambda_1, \lambda_2]$. This interval may be represented as a Heaviside function $H(\lambda-\lambda_1)-H(\lambda-\lambda_2)$. The Fourier transform of this function will give us a pulse in time space, with a pulse width Δt approximately equal to the inverse of the frequency interval Δf tied to the wavelengths by the dispersion relation $c = \lambda f$. For instance, if we mode lock near continuous wavelengths in a interval of 200 nm which would correspond to a frequency interval $\Delta f \sim 10^2$ THz, we can create a pulse with a pulse width of $\Delta t \sim \frac{1}{\Delta f} = 10$ fs.

2.5. Photoelectric effect and charged particle acceleration

The photoelectric effect postulates that the emission of electrons from a material irradiated by electromagnetic waves only occurs past a certain frequency of the waves. The electromagnetic wave consists of photons with energy $E = \hbar\omega$. Emission of electrons occurs if E exceeds the material specific work function W which represents the potential energy needed to extract/eject an electron, which are also called photo-electrons. If the photon energy E is smaller than W, the emission of photo-electrons can still be triggered by multi-photon absorption processes. However, the cross section of multi-photon absorption processes leading to photo-electrons is generally significantly lower than single-photon absorption.

The acceleration of charged particles is achieved through placing it in an electric field. Via Coulomb interactions the charged particle experiences a Lorentz force given by $\vec{F} = q[\vec{E} + (\vec{v} \times \vec{B})]$, where q is the charge of the particle, $\vec{E}$ is the electric field, $\vec{v}$ is the velocity of the particle, and $\vec{B}$ represent a magnetic field. If there is no magnetic field $\vec{B} = 0$, the Lorentz force reduces to $\vec{F} = q\vec{E}$. Objects that create electric fields are referred to as electrodes. Depending on the geometric shape of the electrodes, their positioning relative to each other, and the applied electric potential the course of electric vector field $\vec{E}$ may be manipulated, allowing the acceleration of charged particles in the desired direction.

2.6. Pump probe principles

The pump/probe method allows the investigation of material properties in a state out of thermal equilibrium. The principle of the pump/probe experiments is described as follows. A local excitation of a system is achieved through a pump signal. The pump signal is followed by a subsequent probe signal which passes through the same local excited area and is measured by a detector. The excitation and subsequent relaxation of the system takes place within a specific time frame. To investigate this dynamic process as a whole the probe signal is sent with a variable temporal delay in relation to the pump signal. The probe signal will be altered depending on the current state of the excitation/relaxation while passing the system. By measuring these changes of the probe signal properties of this dynamic process can be mapped. The pump/probe signals take the shape of pulses. Since the recording of the dynamics in the target occurs in snap shots, it is important that the pulse signals have a short pulse width relative to the time scales of the systems relaxation dynamics. Excitations/relaxations that take place on a nanosecond time scale will require sub-nanosecond probe signal pulses for accurate state measurements.

This method of pump/probe was first presented by Ahmed H. Zewail [9], where he used light from lasers to pump and probe the dynamics of molecular motion on the femtosecond scale which leads to chemical bond breaking/formation [9]. In practice there are no limits to which species of particles the pump/probe signal may consist of, as long possible secondary effects of the probe signal on the system are accounted for. Lasers are the ideal choice as pump/probe signals since considerable technological advancements in laser physics has enabled the production of laser pulses with ever smaller pulse widths reaching levels as low as the attosecond regime as of today [23]. The time4ions project aims to conduct pump/probe experiments combining ions and laser light.

3. Experimental setup

Currently the main aim of the experiment is the generation of ion pulses. The methodology used to create these ion pulses are described as follows. A femtosecond laser is utilized and directed into a vacuum chamber onto a cathode (barium oxide coated tungsten disk) to generate photo-electrons. The cathode is part of an electron beam ion source (EBIS) during this process. Upon the creation of photo-electrons, they are accelerated away from the cathode and further into the EBIS via a negative potential gradient. The EBIS itself is submerged in low pressure argon gas. In the EBIS the accelerated photo-electrons collide with the argon atoms, ionizing them. Within the EBIS there are positive potential gradients which accelerate the argon ion out of the EBIS onto a multi-channel plate (MCP). Both the ions and the photo-electrons can be detected, however not at the same time. The whole process is triggered by the femtosecond laser which produces pulsed laser light with a femtosecond pulse width, that photo-electrons which subsequently generate pulsed ions, mounted in a CF-100 double T-cross.

The setup, which has one vertical tube line and 2 horizontal tube lines which is schematically shown in Fig. 3.1. The experiment stands on an end of the vertical tube line with the other end having a turbo vacuum pump attached to it. The horizontal tube lines are in the same plane but shifted to each other by 90°. One of these tube lines is sealed off by a vacuum window for the laser entry while its complementary end is fitted with a pressure sensor. The other horizontal tube line holds the EBIS along with the gas inlet on one end and an MCP on the other end. Around the center of the chamber a mirror is placed which redirects the laser into the EBIS onto the cathode. During the course of the experiment we have utilized the electron beam ion source (EBIS) in two distinct variations. In the first variation which we call the half-EBIS setup and the second variation called the full-EBIS setup. Both setups have their advantages and disadvantages, which are discussed in the following sections.

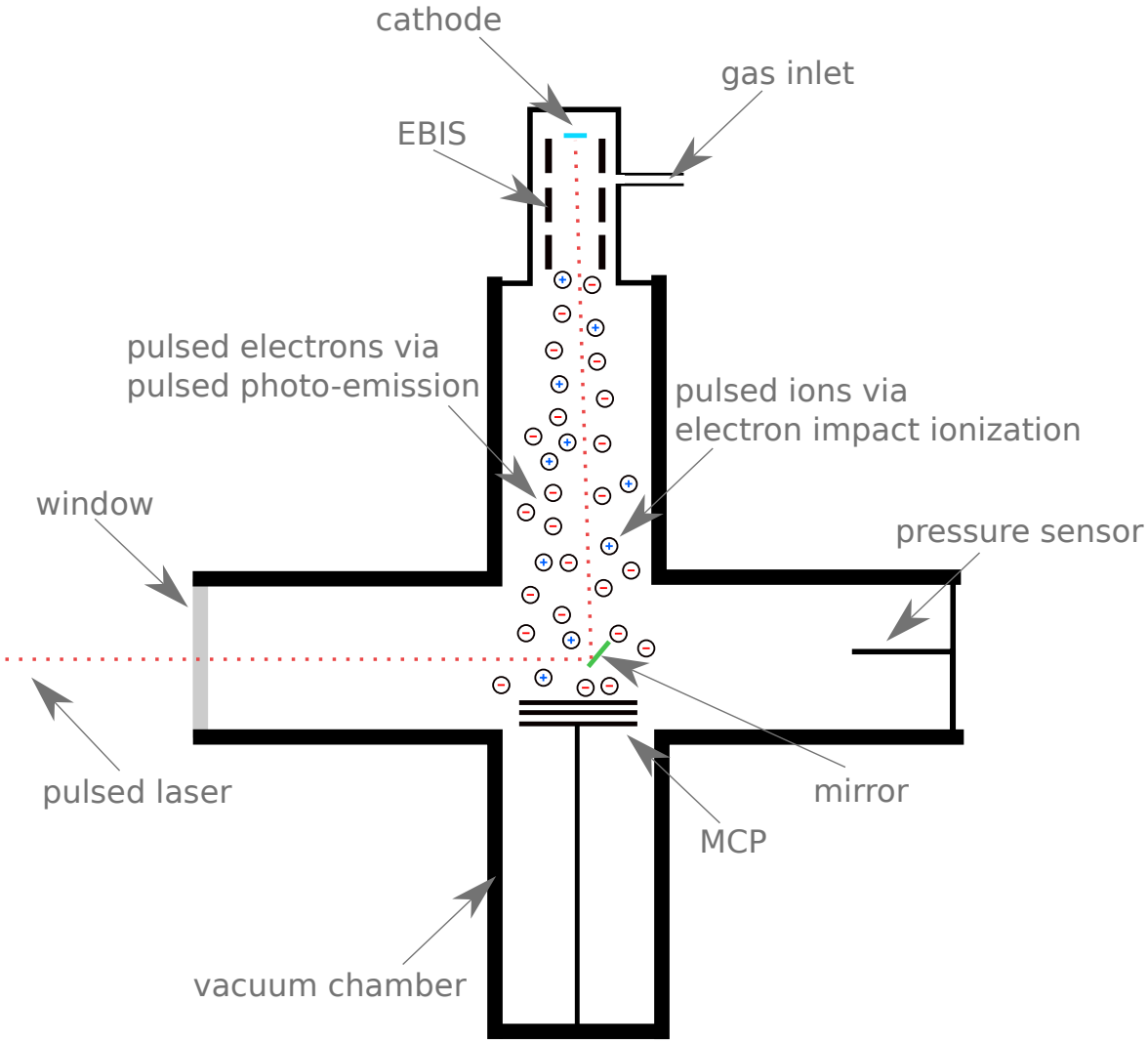

Figure 3.1.: Schematic diagram of the vacuum chamber in experimental setup. A pulsed laser beam is directed into the vacuum chamber through a window. A mirror slightly off beam axis in the center of the chamber redirects the laser beam into the EBIS onto the cathode. The pulsed laser beam induces pulsed photo-electron emission. Next to the EBIS, a gas inlet is mounted, with which argon or nitrogen is let in into the vacuum chamber. These pulsed electrons collide with the gas, and when EII occurs, pulsed ions are produced. The ions or electrons are accelerated towards the MCP by the EBIS, depending on the polarity of the MCP. Depending on the potential configuration of the electrodes in the EBIS, we may also prevent the electrons from exiting the EBIS. The ions are attracted to the MCP via a negative potential, triggering a signal upon collision. By measuring the time delay between laser pulse and the ion pulse, we derive the pulse width of the ions.

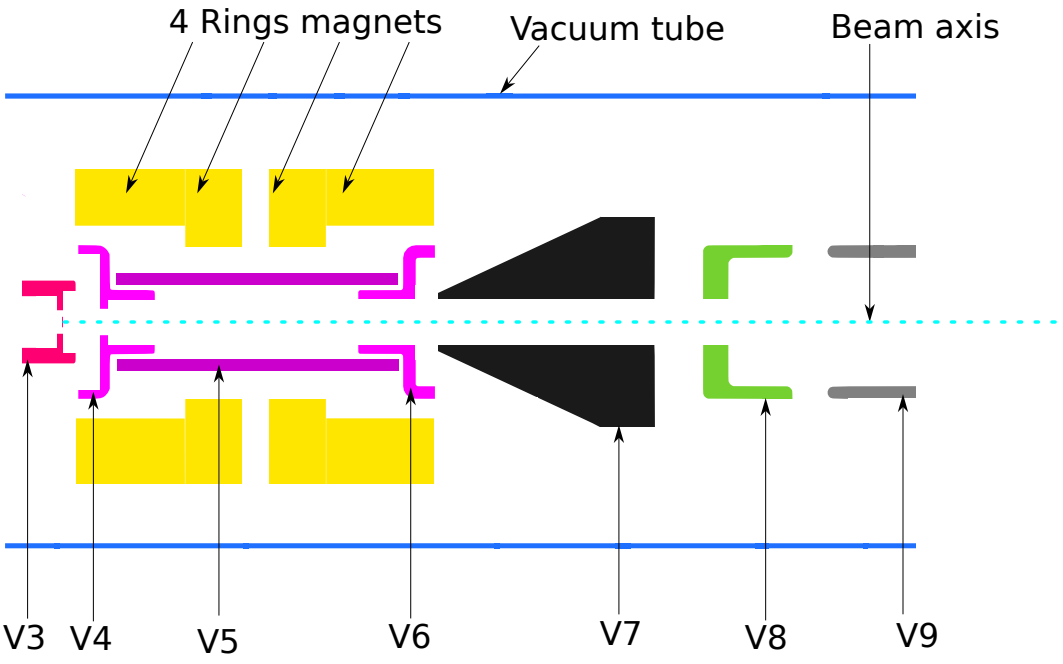

Figure 3.2.: Electrodes in the EBIS. The EBIS consists of an array of electrodes, each serving a different purpose. The first electrode labelled V3 is where the cathode is housed. A negative potential applied to V3 accelerates the electrons originating from the cathode further into the EBIS. The electrodes V4 to V6 are the drift tubes. These drift tubes are utilized to accelerate the ions created by EII. The V7 and V8 electrodes are called the collector and repeller. These two electrodes enable us to prevent the electrons from exiting the EBIS. The repeller has a negative potential applied and the collector is permanently grounded. As such the repeller redirects the electrons onto the collector where they are absorbed. Electrode V9 is also grounded. The ring magnets of the EBIS are also illustrated. The ring are place around the drift tubes V4 to V6.

3.1. Full-EBIS

The full-EBIS setup incorporates all electrodes of the EBIS and is illustrated in Fig. 3.2. The electrodes are labeled from V3 to V9. The dimensions of the EBIS are compact with an inner diameter of 2 mm for V7 to a 5 mm diameter for V6. With such small dimensions one can reliably assume the potentials at the positions of the beam axis that to be equal to the potentials applied to the electrodes at those positions. For instance the potential at the beam axis at the V4 position is equal to the potential applied to the V4 electrode. All electrodes have a distinct purpose in the EBIS. V3 is the electrode in which the cathode is placed and is positioned near the tip of the V3 right at the the base of its conical opening. V3 is set at a negative potential. V4 to V6 are the 3 drift tube electrodes of the EBIS. The main properties of the exiting particle beam is set by these 3 electrodes. The EBIS was initially designed to create a highly charged ion beam. The particle trap configuration is achieved through setting the V5 electrode at a potential lower than V4 and V6 potentials. In this configuration we have a positive gradient between V4 and V5, and a negative gradient between V5 and V6. Both gradients accelerate positive charges towards the center of V5. Here the positively charges (ions) are subjected to a continuous EII process, resulting in high ionization charges. V4 and V6 have a near identical geometry, the main difference is the V4 electrode has an additional protruding ring feature in its shaft which cuts off any negative gradient from V3 entering the trap. Through a certain amount of leakage current through the gradient between V5 and V6 the highly charged ions can exit the EBIT. For our aim of generating ion pulses with as short as possible pulse widths we repurpose the EBIT as fast pulsed source EBIS (FPS-EBIS). We do this by implementing high positive gradients in our EBIS, inducing high ion acceleration rates. The reasoning behind this configuration is the hypothesis that the faster the ions can exit the EBIS, the shorter their time of flight (TOF) before they hit the MCP. With shorter TOFs the ions have less time diverging away from the beam axis resulting in smaller TOF spreads. Since the beam axis resembles the shortest path between EBIS and MCP in our experiment, a higher divergence of ion flight paths away from the beam axis results in overall longer flight paths, and by direct relation a higher TOF spread (pulse width). Combining high gradients with an ion energy filter would also allow us to select ions created within sub μm intervals along a gradient. This selection reduces the overall energy spread of the detected ions, this should lead to a direct reduction in TOF spread. Energy filtering comes at a cost of discarding a significant number ions outside the selected energy window. Electrodes V4 to V6 are usually set at positive potentials. Moving on to the next electrode, we have the V7 collector electrode. This electrode is electrically grounded and features a long shaft with a small diameter. V8 is the repeller electrode set at negative potential. If the negative potential of V8 is lower than the cathode potential V3, then the electrons coming from the cathode do not have enough energy to overcome

the gradient between V7 and V8 resulting in a 180° velocity redirection of the electrons. These electrons hit and are absorbed by the collector. The collector and repeller together ensure that electrons do not exit the EBIS, which could lead to unwanted argon ionization outside the EBIS. The last electrode V9 like V7 is also a grounded electrode. This electrode neutralizes any residual fields coming from the EBIS, the trajectories of the exiting particles are not further influenced by the EBIS gradients. V7, V8, and V9 together may also be used as an einzel lens system with which we can focus the ion beam.

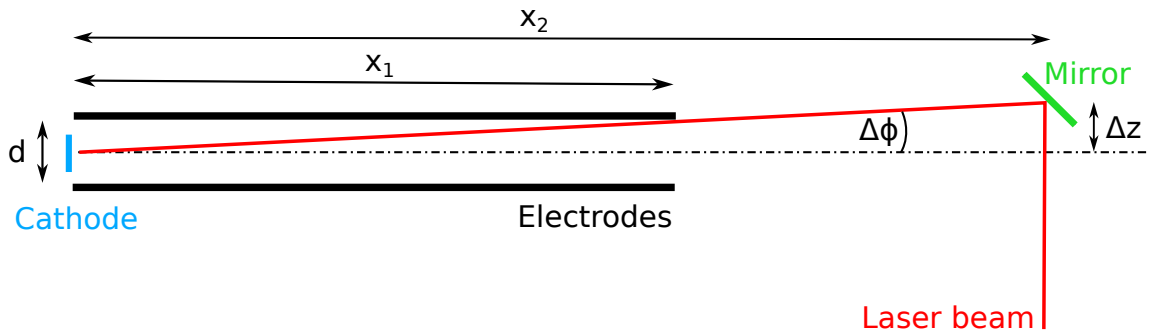

Figure 3.3.: Schematic of mirror (green) alignment in the vacuum chamber. The mirror has to be place off the beam axis (dashed-dotted line) so as to not cut out the pulsed ion beam. Depending on whether we are currently using the half- or full-EBIS setup the mirror alignment faces different constraints. d indicates the smallest inner diameter in the EBIS. x_1 is the distance from the cathode to the further away edge of the electrode with inner diameter d. x_2 is the distance from the cathode to the mirror. $\Delta\phi$ in the maximum opening angle between beam axis and electrode edge. Δz is the maximum length we may offset the mirror away from the beam axis with out cutting off the laser beam (red line) going into the EBIS.

The advantage of the full-EBIS setup is that we can stop the electrons from exiting the EBIS, preventing possible EII of argon outside the EBIS. The disadvantage is that the full EBIS setup heavily restricts the mirror placement in the vacuum chamber. Since the laser beam is to be lead through the EBIS every additional electrode on the EBIS reduces the angular freedom of the mirror plane (see Fig. 3.3), which requires very accurate mirror positioning. The most simple optics configuration for the experiment would be feeding the laser beam through the center of the window and perpendicular to the window plane into the vacuum chamber. Placing the mirror in the center of the vacuum at a 45° angle, would redirect the laser beam by 90°. After this redirection the laser beam and the beam axis of the EBIS are not just parallel but identical. The laser beam can shine directly down the EBIS and onto the cathode. In this configuration

however at least a part of the mirror itself lies in the path of the beam axis. Running the experiment like this would have the mirror blocking a significant portion of the ion beam. We circumvent issue by shifting the mirror slightly away from the beam axis by Δz and reducing the angle by $\Delta\phi$. The maximum amount of Δz we can shift the mirror away from the beam axis is given by angle reduction $\Delta\phi$. The maximum of $\Delta\phi$ (opening angle) is determined by the distance x_1 of the cathode plane to the electrode with the lowest inner diameter that is the furthest away from the cathode. In the full-EBIS setup this is the electrode V8. The most distant point at the lowest diameter $d = 2$mm is $x_1 = 52$ mm. By use of the trigonometric functions we can calculate $\Delta\phi \approx 1.1°$, with $90° - \Delta\phi \approx 88.9°$. Since any angle change the mirror doubles the reflection angle change of the laser beam we can deduct the maximum angle reduction of the mirror plane to be $\sim 0.55°$. The distance x_2 from the cathode to the center of the vacuum chamber where the mirror is placed is $x_2 = 215$ mm. We calculate Δz as follows:

$$\Delta z = x_2 \cdot \tan(\Delta\phi) \approx x_2 \cdot \Delta\phi \approx 4 \text{ mm}. \tag{5}$$

We may shift the mirror 4 mm away from the beam axis. These calculations are done with the idealistic assumption of the laser beam being one dimensional. Since a real laser beam has radial spread we can only shift the mirror by $\Delta z < 4$ mm, the exact amount depending on how much of the laser beam we want to focus on the cathode. The tolerances are to small for a free eye tuning. To simplify this step we constructed a dummy EBIS for the laser alignment process. The dummy EBIS is a tool with the dimensions of the EBIS outlet aperture and cathode position as a hole in the correct distance. As such it allows us to mimic the real EBIS for beam alignment. The dummy EBIS has open ends, if the mirror placement was tuned correctly the laser beam will shine entirely through the dummy EBIS and become visible behind the dummy EBIS outside the vacuum chamber. The dummy EBIS is than exchanged with the actual EBIS which has the laser aligned directly on the cathode.

3.2. Half-EBIS

Removing the V9, the repeller (V8) and the collector (V7) electrodes from the full-EBIS setup gives us the half-EBIS. The advantage of the half-EBIS setup is considerably larger opening angle $\Delta\phi$ for the laser beam redirection which results from the exclusion of the repeller and collector which are the electrodes with the lowest inner shaft diameter. The V6 electrode is now the element furthest away from the cathode. At a distance $x_1 = 27$ mm of the last edge of its inner shaft with inner diameter $d = 3$ mm. Using the same methods as in the previous section, the opening angle of the half-EBIS setup is calculated to be $\Delta\phi \approx 3.2°$. As such the half-EBIS setup provides much more leeway in tuning the mirror compared to the full-EBIS opening angle.

The disadvantage of the half-EBIS is its inability to prevent electrons from exiting the EBIS, since the electron filtering is predominantly done via the collector and repeller. This may lead to argon ionization outside the EBIS, which may distort the ion pulse signal.

3.3. EBIS Magnets

The EBIS is additionally fitted with 4 axially polarised ring magnets positioned on the outer shafts of the V4 to V6 electrodes (see Fig. 3.2). These magnets produce a rotational symmetric field with field vectors close to the beam axis being exclusively parallel or anti-parallel to the beam axis. This field keeps charged particles focused in close proximity to the beam axis. Ideally ensuring most argon ionizations to happen near the beam axis, which should result in less variation in the ion pulse width. The collector V7 cancels out the magnetic field at its tail end (see Fig. 4.3). Since electrons are not being magnetically focused anymore, this increases their likelihood to deviate from the beam axis and absorbed by the collector when redirected by the repeller V8.

3.4. Peripherals

The experiment is supported by a sizable number of peripheral instruments.

1. Optical gadgets
   An optical array is used to guide the laser beam into the vacuum chamber. This array features fully reflective mirrors, beam splitters, an adjustable periscope, beam reducer/expander, and focusing lenses. The beam splitters are used to siphon a fractional portion of the laser beam, which is fed to the photo receiver and the spectrometer. Following the beam splitters in the array we arrive at the adjustable periscope. Since the initial laser beam and the beam axis are not at the same altitude, the laser beam height is leveled to the beam axis height with the periscope. The final element in the optical array is the beam reducer/expander. We use the beam reducer to shrink the laser beam radially. A small laser beam diameter enables us to direct more laser light into the EBIS at steeper angles which would otherwise be blocked off by the electrode walls.

2. Photo receiver
   We use an ultra fast photo receiver to pick up the femtosecond laser pulses from the laser. The pulses picked up by the photo receiver are sent to the discriminator

for further signal manipulation. The laser pulses picked up by the photo receiver is used as start or stop signals of our ion/electron pulse TOF measurements.

3. Spectrometer
   The spectrometer is used to inspect the spectral form of the laser which is needed for the preparation of before mode locking. In the non mode-locked state the laser beam is a monochromatic continuous wave, corresponding to one peak in the wavelength spectrum. This peak has to be shifted to an appropriate wavelength region before the laser can engage the mode-lock state.

4. Discriminator and rate divider
   The laser pulses picked up by the photo receiver are sent to the discriminator which sends out a NIM pulse in response to the laser pulse. NIM pulses are required to trigger start and stop events for the time-to-digital converter (TDC). We additionally include a rate divider between the discriminator and the TDC. The purpose of the rate divider is to limit the amount of NIM pulses sent to the TDC, otherwise the femtosecond laser with a repetition rate of close to 74 MHz fills our data files with junk data points.

5. Amplifier and voltage coupler
   The detector setup consists of 2 multi-channel electron multiplying plates (MCP) in the chevron configuration, followed by an anode plate (see Fig. 3.4). All plates are set at certain potentials depending on the particle type one wishes to measure. At the anode the particle signal is picked up as a voltage pulse . The anode is set at a potential through a voltage coupler and is furthermore hooked up to an signal amplifier since the MCP signal can be very small due to low particle fluences in the experiment.

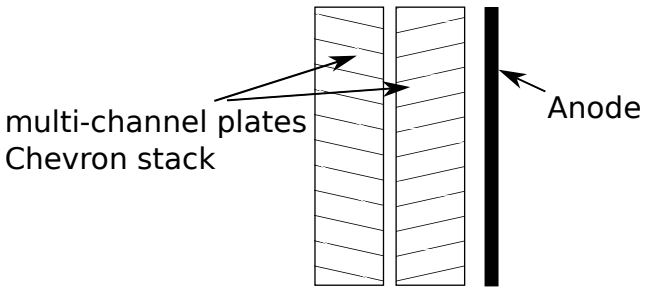

Figure 3.4.: The illustration shows the schematic setup of our particle detector. The detector consists of 2 multi-channel electron multiplying plate in a chevron stack followed by an anode plate.

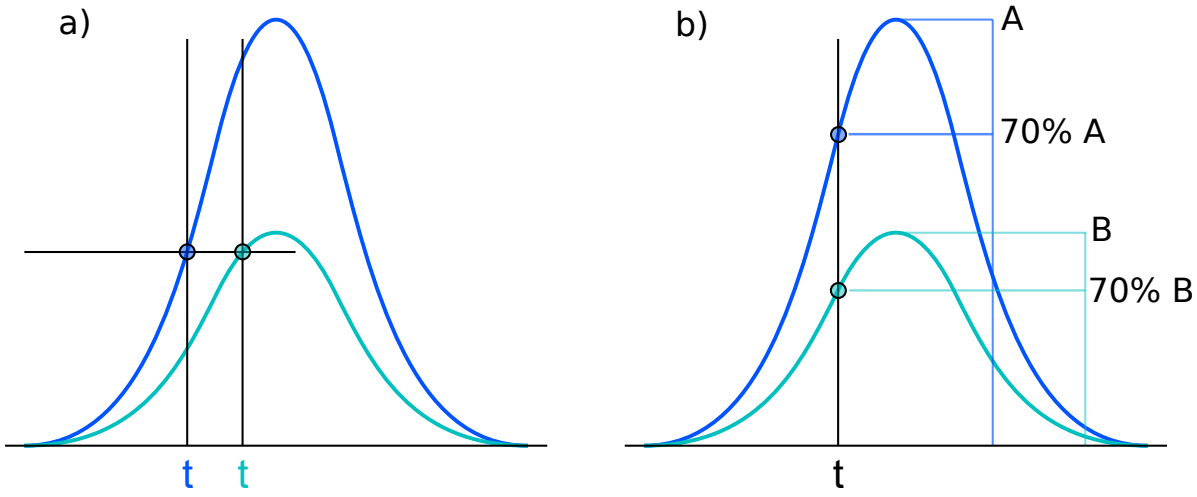

Figure 3.5.: The illustration shows the triggering times induced by a signal. a) if the signal exceeds the threshold value a timing event is triggered, for signals with differing heights event are triggered at different times t. b) when the signal reaches a constant fraction of the signal maximum value a timing event is triggered. Signals with differing height have the same trigger time t [24].

6. Constant fraction discriminator
   The MCP signal is passed through a constant fraction discriminator (CFD) before a subsequent NIM pulse is sent to the TDC to trigger an event. The CFD evaluates the MCP signal and triggers a NIM pulse when a set fraction of the maximum of the currently evaluated MCP signal is reached. This process ensures that TDC events are triggered at equivalent moments between varying MCP signal heights and shapes (see Fig. 3.5).

7. Time-to-digital converter
   Both start and stop signal of the experiment are brought together at the time-to-digital converter (TDC) where time-of-flight measurements are recorded. The TDC requires NIM pulses as event triggers. For this reason multiple discriminators are included among the experiment peripherals.

4. Simulation setup

4.1. Ion trajectory simulations with Simion

In parallel to the real experiment I also carry out the experiment virtually via particle trajectory simulations. Simulations of experiments are a relatively simple and cost effective tool for preliminary testing and exploring of different experimental configurations. Compared to an experiment the parameters in a simulation can be can changed quicker and unlike the experiment the simulation runs at speeds faster than real time.

I conduct ion trajectory simulations via the Simion software package [25]. Simion calculates the electric and magnetic fields of a given set of electrodes which can be described by the Laplace equation. As the Laplace equation in electrodynamics mostly describes electric fields, Simion's capabilities for electric field calculation are much more expansive compared to its magnetic field calculations. However, Simion offers an additional set of tools to implement magnetic fields which cannot be described by the Laplace equation. The Laplace equation is solved via finite difference method in Runge-Kutta algorithms. The fields of the electrodes are calculated in free space and the charged particles are accelerated via the Lorentz Force. Different electrode geometries and configurations may be implemented in Simion. This step is by taking the CAD drawings of the electrodes and converting them into potential array files within Simion. The field calculations is done in the subsequent step called "Refining". For a detailed description of these steps I refer the reader to previous works by the time4ions group [12].

A feature of Simion is that it offers a graphical interface, which provides neat visualizations of the ion trajectories and potential progress. Simion also features the workbench program which enables more control over the simulation than the graphical user interface. I utilize the workbench program feature in our simulations for the automated running of multiple different potential configurations, randomization of particle initial conditions, magnetic field implementation, data recording, and ionization.

The simulations conducted as part of this thesis are an improvement and an extension of simulations I and the time4ions group have done in past works. The main aim of these simulations was a proof of concept that ion pulses with sub nanosecond pulse widths are achievable. These simulations have been done assuming rough approximations for the

experimental conditions. Firstly, hydrogen was chosen as the ion species for simulation instead of argon. The reasoning behind this approximation is that hydrogen interactions being the simplest atom are well researched. Approximating the ionization collision as an elastic collision one can calculate the ion recoil angles for atomic hydrogen. Secondly, the ionization volume in which the hydrogen ions are created has been artificially restricted to a very optimal position along the beam axis between the V4 and V5 electrodes. Last but not least, the explicit simulation of electrons is not included, only their energy and mass as the impact projectile in EII is considered in the determination of initial conditions for the hydrogen. The results of these simulations are very promising since they suggest the feasibility of generating ion pulses with pulse widths in the double digit picosecond range at room temperature and single digit picosecond range and mK gas temperatures [12, 26].

I improve the simulation by including the electrons in the simulation which travel through the EBIS and ionize argon. Detailed descriptions of the improved simulation is given further below.

4.2. Electric and magnetic fields

Configuring the electric fields in Simion is a fast process. Once an electrode assembly has been converted to potential arrays and refined, they can be imported into a workbench. In Simion the workbench is the work space including the GUI and the visualization of the electrode assembly. Each electrode has an assigned variable name within Simion. The "fast adjust" feature allows me to choose the potential values and apply them to the variables. The potential and field calculations in free space around the electrodes are then done by Simion. A visualization of the electric potential progression of the EBIS is shown in Fig. 4.1 with potential configuration V3 = −1 kV, V4 = 5 kV, V5 = 3 kV, V6 = 1 kV, V8 = −2 kV, and V7 = V9 = 0 are always grounded.

The inclusion of the magnetic fields into Simion is a little more complicated than for electric fields. In Simion any electric field can be reconfigured as a magnetic field. This means any magnetic fields which can be described by the Laplace equation are fairly easy to implement. However, a large number magnetic fields do not fulfill this criteria. As such Simion offers tools within the workbench user program with which one can script in more common types of magnetic fields or if magnetic data is available Simion can read in the magnetic field data.

The EBIS is fitted 4 ring magnets which are axially polarised. The axial polarisation

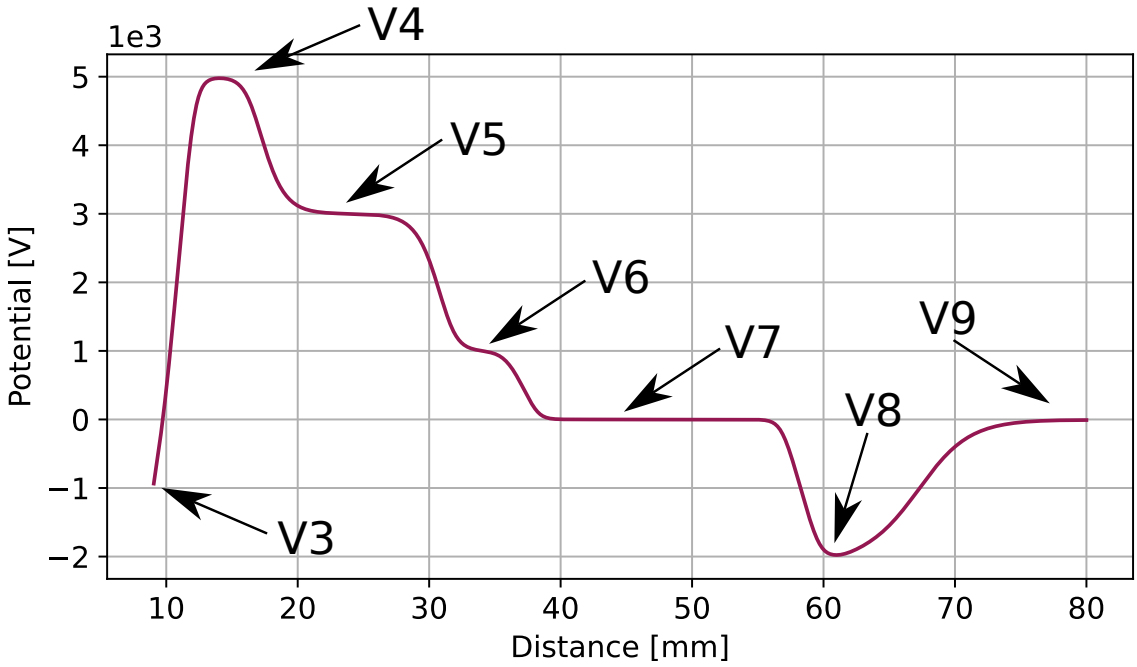

Figure 4.1.: Potential slope progression through-out the EBIS along the beam axis. 0 indicates the ground level. The following potential configuration was set at: V3 = −1 kV, V4 = 5 kV, V5 = 3 kV, V6 = 1 kV, V8 = −2 kV. V7 and V9 are always on ground. First I have steep increase in potential from the cathode V3 to the first drift tube V4. Between V4 and V7 I can set multiple gradients. With the repeller V8 I can trap the electron in a potential well between the cathode and the repeller itself. If V8 < V3, electrons are trapped with in the EBIS. If V8 > V3, then the electrons gain enough to pass the repeller. V7, V8, and V9 may also be utilized as an einzel lens system for focusing the ion beam.

of the ring magnets provides a field which has close to no radially directed components in the inner space of the EBIS. In previous simulations I implemented a coil around the EBIS to generate a magnetic field. This represents a rough approximation of the field produced by the actual ring magnets of the EBIS. A number of steps need to be done before it can be read into Simion such as the alignment of origins between data and existing EBIS simulation, the number of grid cells and step intervals of the magnetic field needs to be evaluated, and the data must be configured as cylindrical if only axial and radial field components are given. The field components need to be exported to a new file along with a configuration header so Simion knows how the data is to be read.

In Fig. 4.2 an example is given. The figure shows two files. The lines of the first

a)

```
1  fieldx,fieldy,fieldz,"field_array{nx=501,ny=41,nz=1,symmetry='cylindrical',
2                                   mirror='y',dx_mm=1/5,dy_mm=1/10,dz_mm=1/10,
3                                   potential_type='magnetic',rt=0,el=0,az=0,
4                                   scale=1,x=-10.25,y=0,z=0}"
5  0.0590093600,-0.0000001078,0.0000000000
6  0.0599418000,-0.0000000572,0.0000000000
7  0.0608948800,-0.0000000658,0.0000000000
8  0.0618673400,-0.0000001191,0.0000000000
9  0.0628565600,0.0000001040,0.0000000000
```

b)

```
164  -- Load field interpolation support.
165  local FieldArray = require "simionx.FieldArray"
166
167  -- Load solenoid field from data file.
168  local field = FieldArray("SimionReady_mike_bis_r=4_mitK.csv")
169
170  -- Override magnetic field in magnetic PA instances
171  -- with that in the field array.
172  function segment.mfield_adjust()
173    ion_bfieldx_gu, ion_bfieldy_gu, ion_bfieldz_gu =
174      field:get(ion_px_mm, ion_py_mm, ion_pz_mm)
175
176    ion_bfieldx_gu, ion_bfieldy_gu, ion_bfieldz_gu =
177        ion_bfieldx_gu*1e4, ion_bfieldy_gu*1e4, ion_bfieldz_gu*1e4
178
179  end
```

Figure 4.2.: Two file snippets are shown. a) The first file from lines 1 to 9 shows part the magnetic field data file. Lines 1 to 4 contains read instructions for Simion. This header tells Simion how the magnetic field data is formatted. b) The second file from lines 164 to 179 is the code snippet used to read in the data. First support software is loaded. Then the field is read in. Depending on the where the ion currently is in the simualtion the magnetic field at that point to retrieved. Since the magnet field is given in Tesla is has to be converted into Gauss (Simion requires magnetic fields be given in Gauss).

file are labelled from 1 to 9. The lines of the second file go from 164 to 179. Lines 1 to 4 is the header of the file. These lines let Simion know how to read the magnetic field data. The first 3 comma separated values (csv) of the header indicate where the magnetic field components are written. The last value "field_array..." gives additional information. The nx, ny, nz options tells Simion in how many points in each dimension the magnet field components are given. Since the magnetic field is cylindrical one has to set the symmetry accordingly. The mirror option tells simion to the cylindrical symmetry is in the y,z plane. The options dx_mm, dy_mm, dz_mm sets the distance

between the points nx, ny, nz. The magnetic field in-between these points is linearly interpolated. The next option determine the potential type and remaining options lets me set the orientation, scale, and origin of the field. From line 5 onwards the magnet field components for each point is given. The z-components are all zero, since they are already given by the y-components (cylindrical symmetry). Lines 164 to 179 are the read-in commands in the user program file of Simion. Line 165 reads in the software package with which one can declare field arrays. Line 168 reads in the magnetic field data (= First file, Line 1 to 9 in Fig. 4.2). Lines 172 to 179 sets the magnetic field in the simulation depending on where the ion currently is positioned (lines 173-174), and adjusts the magnetic field units from Tesla to Gauss (lines 176-177). Simion requires that magnetic field be given in Gauss. The magnetic field data provide to me is given in Tesla.

The magnet field component in beam axis direction along the beam axis of the EBIS is shown in Fig. 4.3. As one can see the magnetic field is zero at he cathode. In the middle the second drift tube (V5) there is a little dip due to the gap in the ring magnet at that position (see Fig. 3.2). The collector electrode (V7) manages to reduce the magnet field at its tail end. This shielding is meant to cancel out magnetic focusing of particles between the collector and repeller. Without magnetic focusing, electrons are more likely to deviate from the beam axis eventually colliding with the collector and being absorbed.

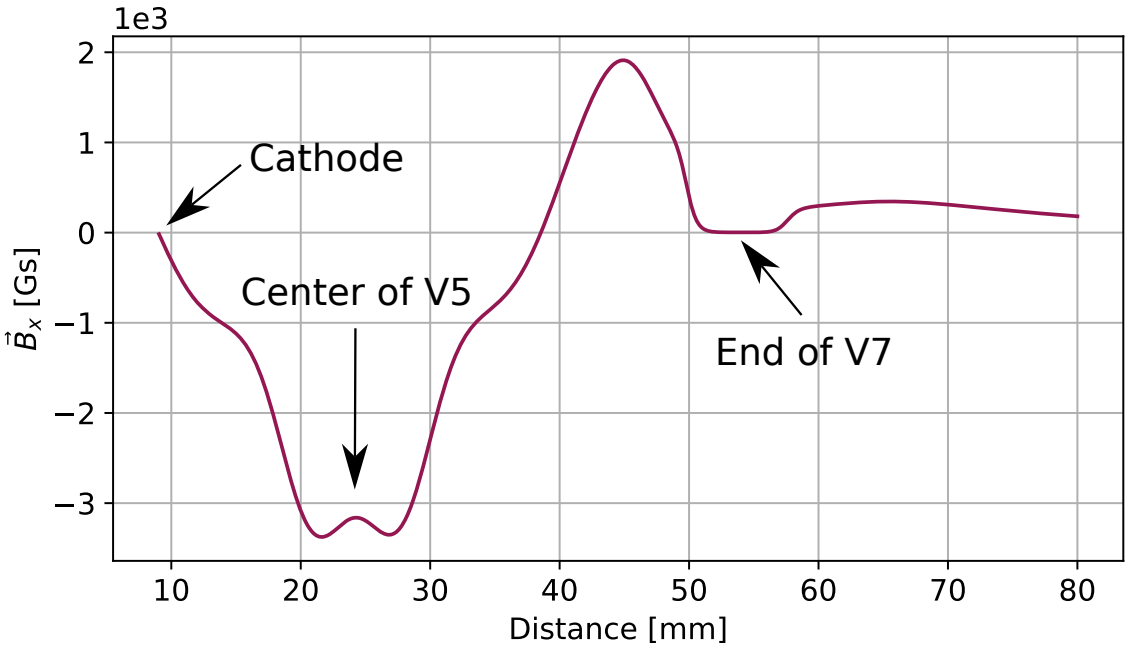

Figure 4.3.: Magnitude of magnetic field vector component in the beam axis direction along the beam axis. The magnetic field at the cathode is zero. In the center of the second drift tube V5 there is a dip in the field due to the little gap in between the magnets (see Fig. 3.2). One can see that the collector manages to cancel out the magnetic field at its tail end.

4.3. Electron Implementation

As mentioned at the beginning of this chapter, I now include the simulation of electron trajectories in our work providing a significant improvement to the simulations. The generation of electrons with initial conditions works in a similar manner as the generation of the hydrogen ions in the previous simulations. I have rewritten the "fly2"-file used to create the hydrogen to create electrons instead. The electrons are generated evenly across the front facing surface (towards the EBIS exit) of the cathode which gives me their initial starting positions. The initial momenta of the electrons are calculated via the Maxwell-Boltzmann-distribution. Their directions are isotropic-ally distributed within the front facing half of the solid angle of a sphere. In the experiment the electrons are created by the laser pulse, which has a temporal distribution (pulse width). This implies the electrons must not necessarily all be initially generated at the same time. In previous works, this aspect of the experiment was usually considered in the simulation by setting a distributive time of birth (TOB), corresponding to a derivative of the laser pulse width, for the particles. However, since electrons are directly created by the laser

pulse which has a pulse width of 12 femtoseconds, and Simion time tracking is done in the microseconds, I have chosen to neglect this temporal distribution for electrons TOBs and assume instantaneous creation of all electrons at once.

4.4. Argon Implementation

The implementation of argon is done via virtual EII collisions in the simulation. The difficulty in this virtual EII collision process is the determination of the positional coordinates at which ionization should take place. Ideally one has to account for cross sections, projectile energies, and gas pressure which relates to the mean free path and determines the number of collisions along a projectiles path. In our simulation the pressure dependence is ignored since accurate implementation of the number of collisions at low vacuum would result in relatively few argon ions for which the simulation of a number of electrons magnitudes higher would be required. In the experiment low gas pressures should be reflected in comparatively low numbers of EII collisions. In turn this dependence should determine how long a measurement should take to ensure sufficient particle counts of the measurement. This aspect of the experiment is not considered in the simulation. Since this would be an ineffective use of computational resources I instead chose the number of collisions to be time step dependent. During the electron simulations at every time step the current position of the electron along its trajectory is chosen as a possible ionization point. An internal segment of the code which considers cross sections stochastically determines if an ion is generated at this point. The EII cross sections is dependent on the projectile electrons (see equation 4) kinetic energy and this energy varies through-out its trajectory since the different potential gradients in the EBIS facilitate a constant interchange between kinetic and potential energy during a fly-through (see Fig. 4.1). For virtual EII collisions it is helpful to know an analytic expression of a cross section so one can determine it at any point of the electron trajectory. At EII collisions the projectile trajectory is deviated from its original path. However, in the simulation the virtual EII collisions affects on the electron trajectory are not considered. The reasoning behind this is that in the experiment most electrons do not partake in EII since the rate of collisions is assumed to be very low at low pressures and at most an electron will only encounter one EII collision process during its fly-through before it collides and is absorbed by some object in the experiment. Since those electrons that encounter EII mostly only do it once, their subsequent change of trajectory does not play a significant roll anymore. As such I can effectively simulate ionizations by only having one or a few electrons produce all ions, which I assume will lead to qualitatively the same ion pulse width results as a fully accurate EII simulation would. Once the ionization positions are determined, the momentum of the argon ion is

calculated. For this calculation I rely on the results of McConkey et al. [22] which state that the momentum transfer in EII is most significant for low mass atom species such as hydrogen and helium. Since I am simulating argon, a much heavier atom species, I ignore momentum transfers to the ion by EII. McConkey et al. also measured the recoil angle distribution of singly ionized argon and found distinct peaks at 90° counted away from the ionizing electron beam axis. This distribution was only measured for EII at projectile energies up to 300 eV. I expand the use of this distribution to all projectile energies in the simulation. The argon is given a momentum based on the temperature dependent Maxwell-Boltzmann-distribution for velocities. This velocity distribution, however, is not applied in an isotropic manner anymore, instead I use McConkey's angular distribution. Finally in the simulation, only a few electrons are simulated which set the ionization points along their trajectories at every time step of the simulation. If ionization determined by cross section (Eq. 4) occurs, the ionization position values and thermal momentum values with McConkey's distribution are recorded in a separate "ion"-file. Once the first simulation run of electrons has concluded, the "ion"-file is called by the code and the ions are simulated in a second simulation run. The ion properties at their collision points at the MCP and else where (EBIS) are recorded and the pulse width of the ion pulse is determined. A full detail explanation of the simulation code is provided in App. A.

5. Results

5.1. Experiment

In the experiment we measure TOFs of electrons as well as ions. The experimental results below are shown first for the half-EBIS setup and followed by the full-EBIS setup results.

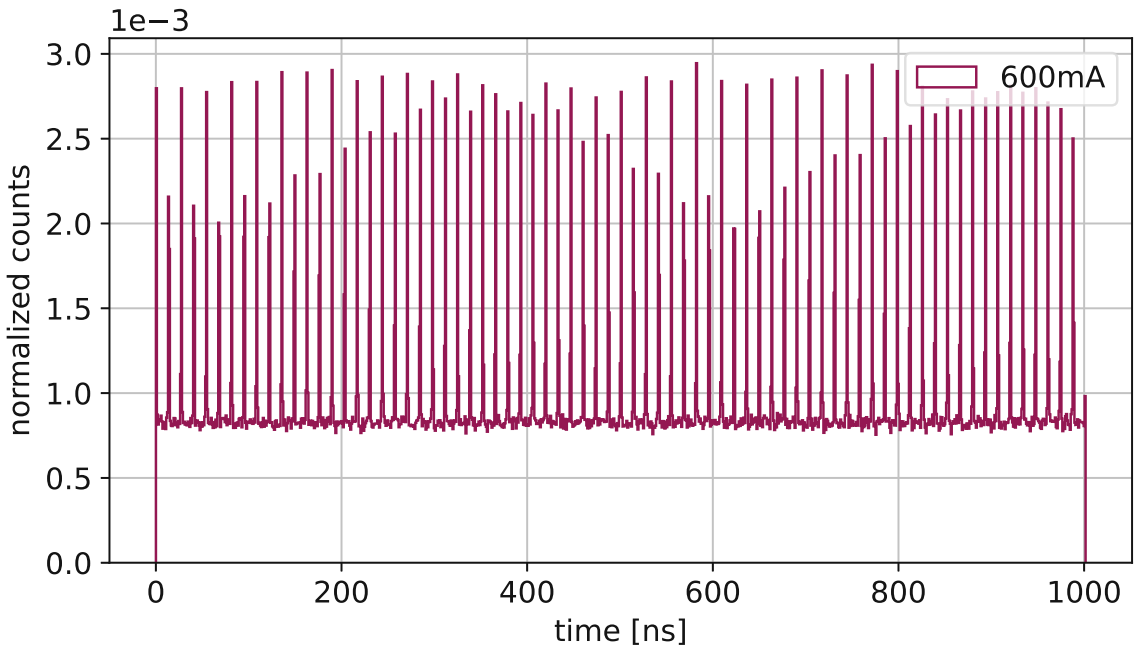

Figure 5.1.: Raw electron TOF distribution measured at a cathode heating current of 600 mA. The laser pulse repetition is rate divided. This means we only use every 74th laser pulse for time triggering. As such we measure TOFs over 1 μs. The plot shows the individual electron pulses generated by the laser. The spectrum shows a wave structure in the peaks heights. This is an artifact caused by the number of bins in the spectrum. There is considerable amount of thermal noise caused by thermally emitted electrons at 600 mA heating current.

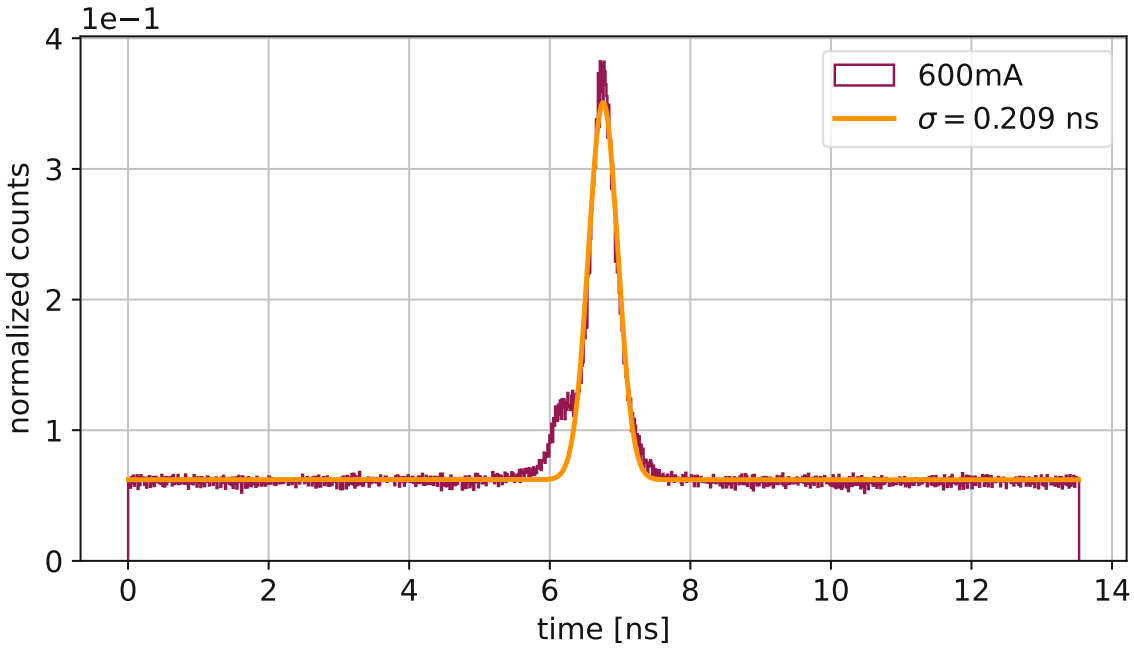

Figure 5.2.: Modulated electron spectrum. Since the electron pulses in Fig. 5.1 are all equidistant, we can bunch them together by dividing their TOF values by the laser repetition period $T = (74\ \text{MHz})^{-1} \approx 13.53$ ns, and only plotting the division remainder. Subtracting the noise, the pulse width is determined at the full width at half maximum of the distribution. The pulse width in the spectrum shown is $2.3458 \cdot \sigma \approx 490$ ps. The origin of small TOF heap on the left on the main pulse is currently unknown.

5.1.1. Half-EBIS Measurements

The half-EBIS setup consists of 4 electrodes (V3-V6) with surrounding magnets. The Collector (V7) and Repeller (V8) are not included. The main advantage is that the mirror used to direct the laser beam into the EBIS can be sufficiently distanced away from the EBIS beam axis, thereby not blocking any particles exiting the EBIS. The main disadvantage is the reduced capability of filtering the electrons from exiting the EBIS, thereby enabling undesired EII outside the EBIS.

Electrons

In Fig. 5.1 a measured electron TOF spectrum produced with the half-EBIS setup is shown. The TOF measurement is started by the electron hitting the MCP and ended by a laser pulse signal. The rate divider in the experiment was set to 74. This means only every 74th laser pulse ends the TOF measurements. This choice was made for the

purpose of being able to detect the laser repetition rate (time structure) directly in the measured spectra, as well as for the reason that the photo-electron emission current has proven to be very small and because the data acquisition rate of our computer cannot keep up with the full laser repetition rate. Every 74th laser pulse results in a stopping trigger frequency of 1 MHz (= 1 μs TOF interval). This measurement was taken at following experimental values V3 = 1 kV, V4 = 4 kV, V5 = 2 kV, V6 = 0 kV, gas pressure of under 10^{-9} mbar at room temperature, and a cathode heating current of 0.6 A. Electrodes V7 to V9 are not included in the half-EBIS setup. The MCP was set to 0 kV on the front plate, 2.2 kV on the back plate, and 2.3 kV on the anode. As can be seen in Fig. 5.1 we have relatively high thermal electron emission shown by the uniform intensity offset from zero intensity (thermal noise). On top of these thermal electrons we have a number of electron peaks. These peaks have a temporal separation of ∼13.531 ns, which corresponds to the lasers repetition rate of ∼73.9 MHz. The spectrum appears to have a beat (Schwebung), this is only an optical illusion which happens when a pattern occurs in the peak division into 2 bins of the histogram TOF spectrum.

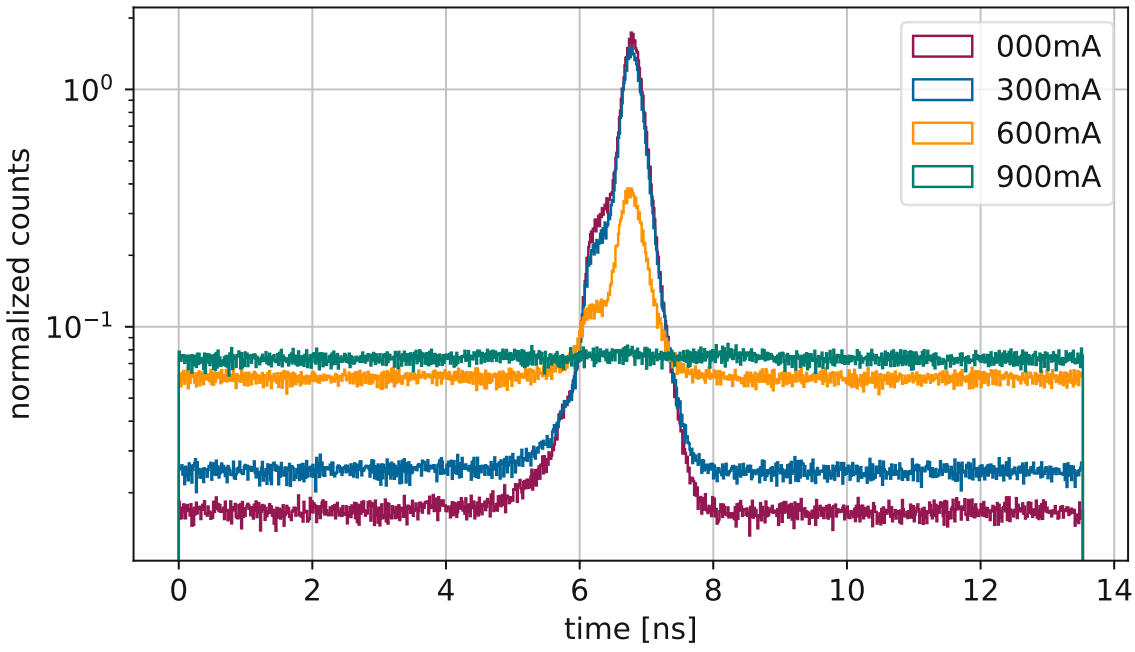

Figure 5.3.: Modulated electron TOF spectra plotted on a logarithmic scale measured at varying cathode heating currents. The pulse shape is best at low heating currents. At 900 mA the pulse is completely overshadowed by thermal electrons.

Since all the peaks in Fig. 5.1 are equidistant to each other we can modulate the spectrum over lapping all peaks. The modulated spectrum enables us to determine pulse widths and thermal noise levels easier. The modulated spectrum is shown in Fig. 5.2. From this spectrum we can quickly estimate the pulse to thermal noise ratio (ptr) and the pulse width (pw). ptr is calculated by the division of the area under the pulse A_p by the area under the uniform thermal noise distribution A_n. In normalized spectra the relation $A_p + A_n = 1$ applies. The thermal noise level is at 0.06 normalized counts. The thermal noise area is calculated to be $A_n = 0.06 \cdot 13.5 = 0.81$ and ptr $= \frac{A_p}{A_n} = \frac{1-A_n}{A_n} \approx 0.23$. In this spectra we have close to 1 pulsed electron for every 4 thermal noise electrons. The pulse width determined by the full width at half maximum of the peak is pw ≈ 400 ps $= 0.4$ ns.

In Fig. 5.3 the electron spectra measured across four cathode heating currents are shown. We can see that highest ptr is achieved at no heating current. However with

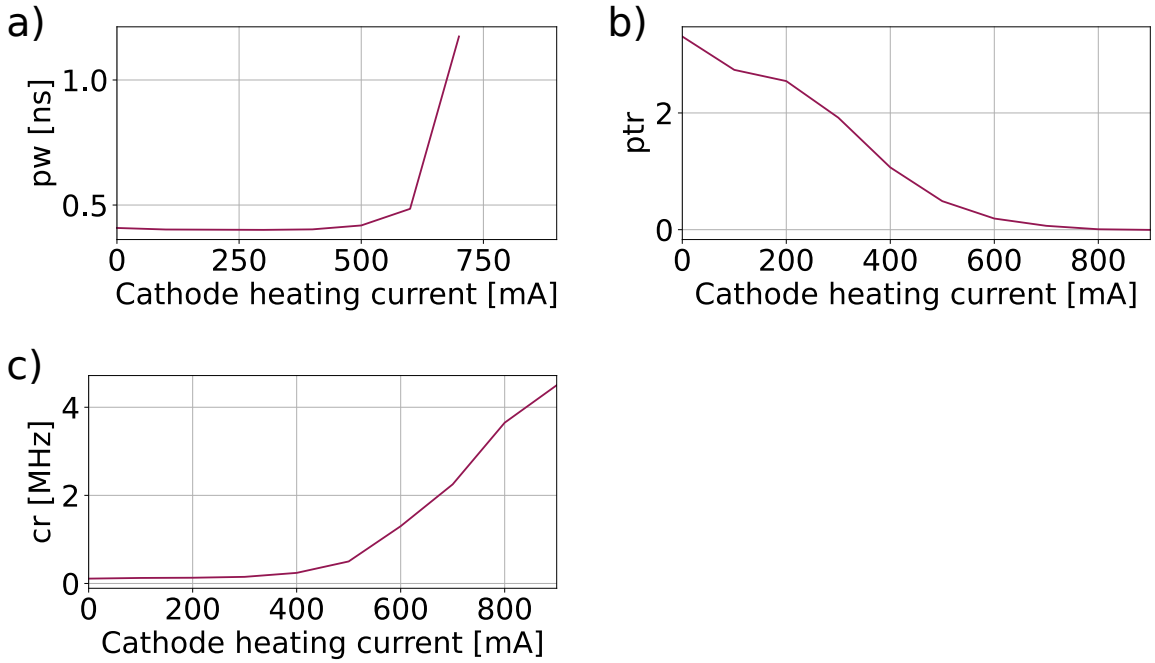

Figure 5.4.: a) Pulse width trend plotted over cathode heating current. We notice a stark increase in pulse width after 600 mA. After this level any pulse information is lost to thermal noise. b) Ratio of pulse counts to thermal counts (ptr) plotted over heating currents. ptr diminishes at higher heating currents. c) MCP count rates (cr) plotted over heating current. The counts registered by the MCP increase with heating current. However, a significant portion of this increase consists of thermal electrons.

no heating current the total emission current is at its smallest. With increasing heating current the pw stays roughly the same however ptr is drastically reduced (see Fig. 5.4) and total electron emission current increases (not shown). The pw shows a drastic increase from 600 mA to 700 mA while the ptr decreases gradually from 0 mA to 900 mA heating current.

In Fig. 5.4 the MCP count rate (cr) over the cathode heating current is shown. In this regard the cathode behaves as expected with increasing heating current inducing an increase in electron output. In these measurements the cathode heating current was gradually increased from 0 to 900 mA, starting from a cold cathode going to a hot cathode. The same measurements have been conducted while ramping down the cathode current, e.g. moving from a hot cathode and measuring during the cooling phase of the cathode. The results of these measurements are shown in Fig. 5.5. The pw remains the same for both types of measurements, however for the slowly cooling cathode the

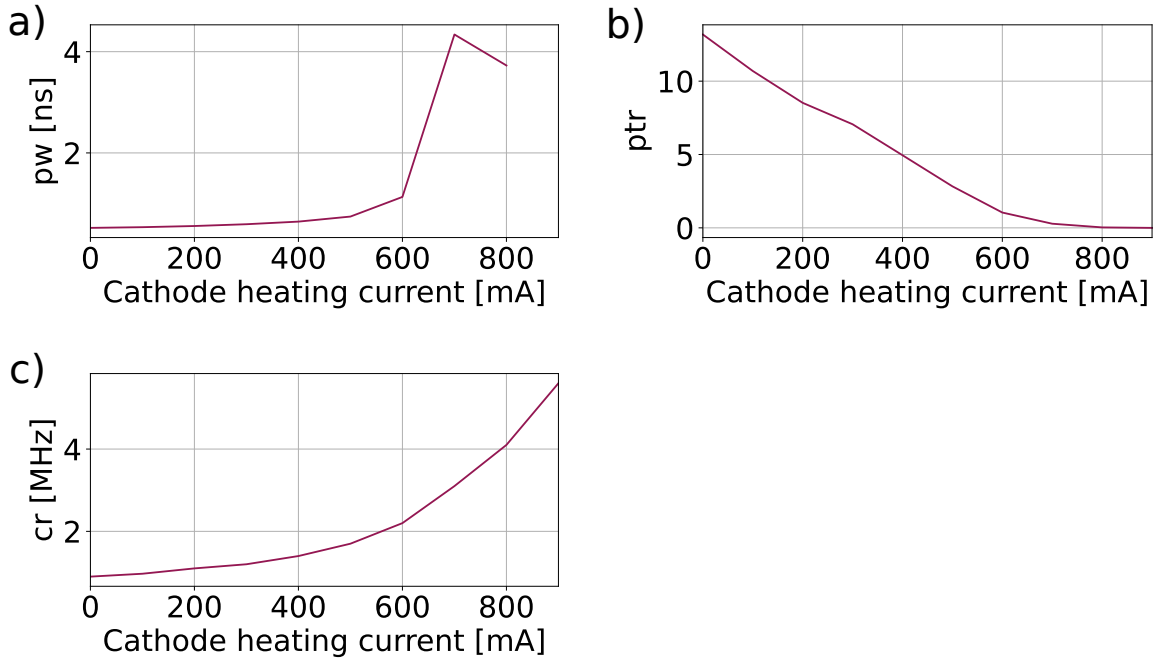

Figure 5.5.: a) pw calculated for measurements taken during ramping down the cathode current. The stark pw increase is shifted from 600 mA to 500 mA. b) ptr plotted over heating currents during down ramping. ptr is significantly better during current down ramp measurements (compare Fig. 5.4 b). c) MCP cr plotted over heating current during down ramping. We get better cr at low heating currents compared the measurements while up ramping the heating current.

pw step is shifted between 500 mA and 600 mA, and we get much better ptr and MCP count rates at low cathode heating currents. However these improvements are short lived and subside once the cathode has had enough time to cool down. It is advised to periodically heat-cool the cathode and measure during this cooling phase. My hypothesis behind the better performance of a cooling cathode with no current flow compared to a current heated cathode, is the assumption that thermal electron emission is mainly caused by the cathode heating current and not the temperature of the cathode. During current flow collision rates between the electrons within the cathode are increased, many of these collisions resulting in electron ejection. A hot cathode with no current flow can be seen as a black body radiator, where the electrons occupy high energy states slowly descending into low energy states during the cooling phase. These electrons occupying high energy states can be easily ejected by the energy gained from the laser pulse, leading to high ptr values.

Measurements have been shown to be volatile depending on the lasers run time. Laser performance fluctuations over long time periods were noticed. In order to classify this volatility we conducted similar measurements as the ones above while having the laser continuously run over long time periods. The measurements were taken on two separate days labelled as D1 and D2 in Figs. 5.6-5.7. On the day D1 measurements were taken straight after the laser was switched on. Afterwards the laser was left running for 3 hours, after which repeat measurements were taken. The same procedure was conducted on a second day labelled D2, where measurements were taken straight after switching on the laser, and than again after 2 hours, and an additional third time after 24 hours of laser run time.

In Fig. 5.6 b) the ptr over all measurements is shown. The ptr is best at no cathode heating current and steadily declines with increasing current. The ptr graph shows that the ptr increases when the laser has been on for at least 2 hours. This property stays consistent over all cathode heating currents. Longer run times of the laser improves ptr at higher heating currents. This behaviour can be assumed to depend on the laser pulse shape. An improving laser pulse shape (less pulse broadening through optical components) would result in better ptr of electrons.

In Fig. 5.6 b) the MCP cr is also shown. The behaviour of the MCP count rate seems to have a inverse trend compared to ptr in regards to laser run time. The MCP count rate increases with increasing heating currents since thermal emission rises with more heating current. The MCP count rate is highest right after the laser is switched on steadily declines with run time. This behaviour suggest the laser power output to decrease over time. This result has been confirmed by direct power measurements of the laser.

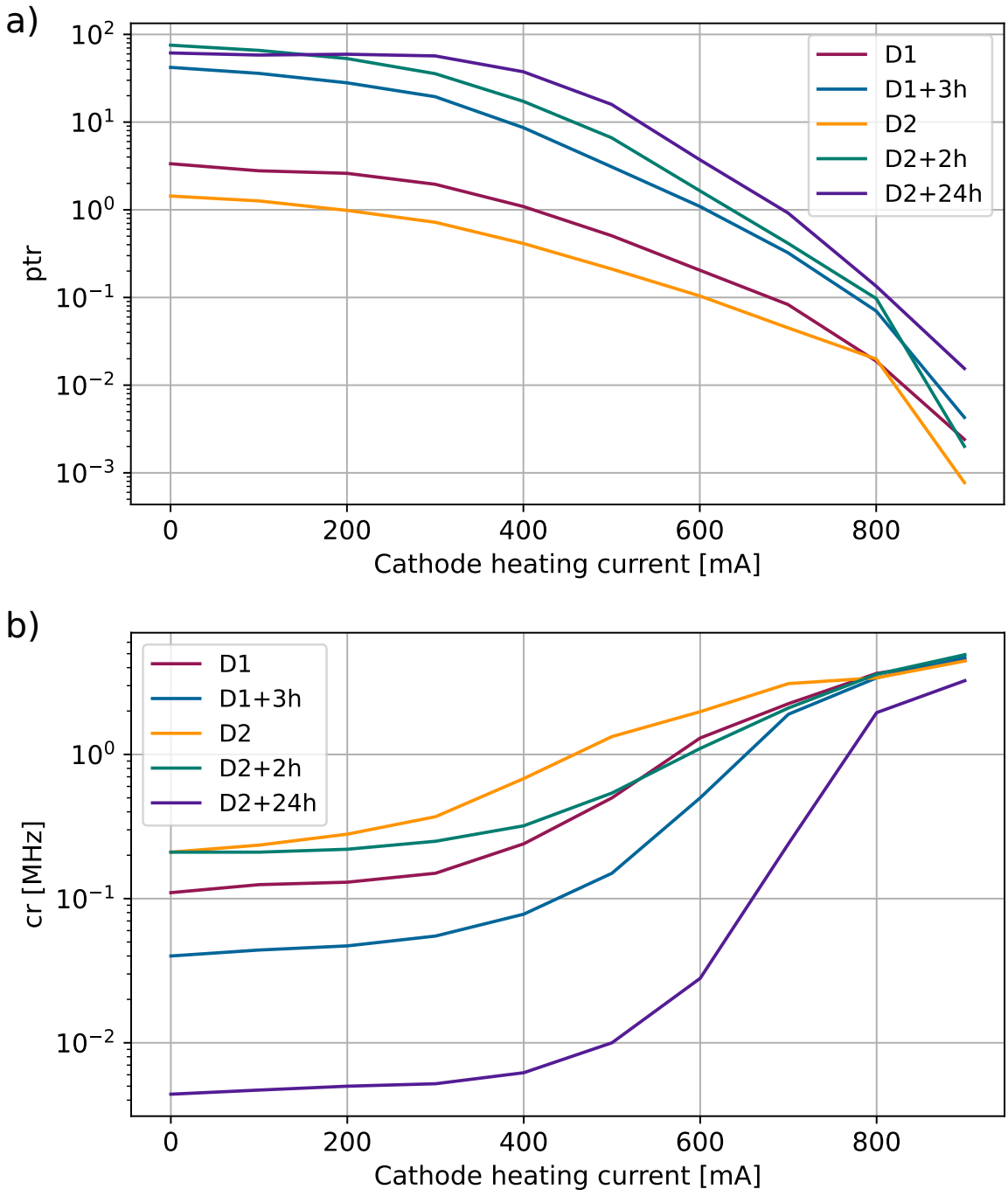

Figure 5.6.: Femtosecond laser performance on BaO coated tungsten cathode a) ptr trend plotted over heating currents. ptr varies depending on how long the laser has been running. b) MCP cr plotted over heating currents and varying laser run times.

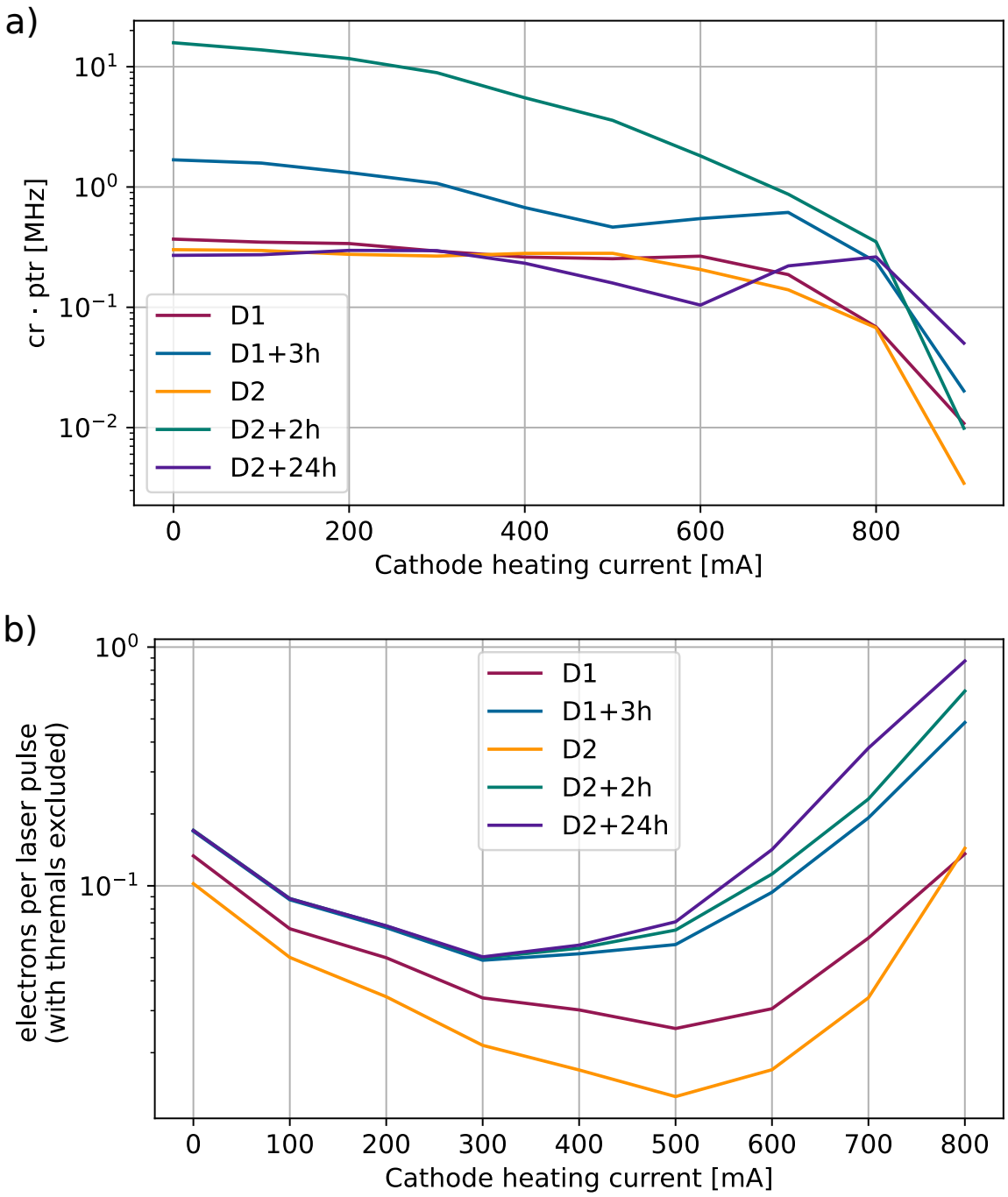

Figure 5.7.: Femtosecond laser performance on BaO coated tungsten cathode a) Index value cr·ptr plotted over heating currents and varying laser run times. b) Pulsed electrons per laser pulse plotted over heating currents (total amount of electrons per laser pulse multiplied with ptr $\cdot(\text{ptr}-1)^{-1}$).

For the creation of ion pulses we ideally want high ptr and a large MCP count rate of electrons. High ptr means we have more pulsed electrons than thermal electrons. The thermal electrons have to be suppressed as much as possible since the only broaden an ion pulse created by EII. However, we also need high electron currents (MCP count rate) to compensate for low EII cross sections. If too few ions are created due too few electrons, measurements over longer time periods would be required for sufficient statistics. In Fig. 5.7 a) an index value graph is shown. The index value is calculated as the product of ptr and MCP count rate. The index is an electron beam quality indicator combining ptr and MCP count rate, the higher the better. Fig. 5.7 a) shows that although more heating current produces higher electron current the quality index is still highest at no heating current and after the laser has been running for at least 2 hours. The index of the the D2+2h measurement is acceptable up to a heating current of 300 mA. All other heating currents and laser run times produce a worse pulsed electron beam. With the present-day pulsed electron emission currents in the experiment, the projected measurement time periods for sufficient statistics is considered to be in the range of days or even weeks.

In Fig. 5.7 b) the amount of pulsed electrons per laser pulse are shown. The thermal part of electrons were filtered out. These plots were calculated by measuring the electron emission current of the cathode at different heating currents and with the laser directed at the cathode. These currents are divided by the elementary charge, with which we get the electron emission frequency. Multiplying the electron emission frequency with the period of the femtosecond laser, we get the total amount of electrons per pulse (pulsed electron and thermal electrons). Multiplying the total number of electrons per pulse with $\frac{\text{ptr}}{1+\text{ptr}} = A_p$, we get the number of pulsed electrons per laser pulse (thermal electrons excluded). Fig. 5.7 b) shows the highest number of pulsed electrons at high heating currents. However, the pulsed electrons in this area are vastly outnumbered by thermal electrons, which completely distorts any ion pulse created by them. The second highest value is at zero heating current, however here we only have 1 pulsed electron every 5 to 10 laser pulses. Due to this low value of pulsed electrons combined with a low EII cross sections for the electron energies in this EBIS configuration, makes the gathering of sufficient data for ions at zero heating current hard to achieve. Laser run time also has a slight influence in this behaviour, generally increasing the pulsed electron efficiency over run time most noticeable at high heating currents. We use a barium-oxide coated tungsten cathode with a work function between 1 eV and 1.8 eV, while our femtosecond mode-lock laser emits photons with energies below 1.7 eV. This implies that we may be relying on multi-photon emission processes to create photo-electrons, which could be the reason for low photo-electron currents.

Ions

The ion spectra shown here have been measured with similar parameters as the electron spectra above (rate divider at 74, ions trigger the start of TOF measurement). Fig. 5.8 shows an already modulated ion TOF spectrum taken with the half EBIS potential configuration of V3 = −1 kV, V4 = 4 kV, V5 = V6 = 0 kV. The MCP potentials were set at -2 kV, 0 kV, 70 V (front plate, back plate, anode). The cathode heating current was set at 500 mA (below thermal electron emission threshold). The ion species is argon, at a high pressure of 10^{-5} mbar, to maximise collision probability between electrons and argon. These settings resulted in a MCP count rate of $\sim$ 40 Hz, and spectrum was measured for 600 seconds.

Fig. 5.9 show the same measurement was taken at a lower pressure of $5 \cdot 10^{-6}$ mbar. The idea behind this measurement was the assumption that high argon pressures do not only lead to higher probability of EII collisions but also lead to higher probability of collisions among the argon particles themselves, such argon ion on argon collisions would contribute to pulse broadening. The spectra in Fig. 5.10 was taken at a cathode heating current of 200 mA. As shown for the electrons, their ptr is higher at low heating current which corresponds to a cleaner electron pulse. A cleaner electron should ideally also produce a cleaner ion pulse.

The spectrum shown in Fig. 5.11 was with half EBIS potentials V3 = −1 kV, V4 = 5 kV, V5 = 3 kV, V6 = 1 kV. A cathode heating current of 500 mA and an argon gas pressure of $5 \cdot 10^{-6}$ mbar. This measurement differs from the other ones by the split of the potential slope in the EBIS. In spectra 5.8 to 5.10 there is only one positive ion accelerating potential gradient between V4 and V5. Previous computational work has shown one potential slope to be the optimal configuration for short ion pulses. However, since these measurements proved to be unfruitful we attempted the split potential configuration. In this spectrum small peak (pulse) structures can be distinguished at TOF times at 5 ns, 7 ns, and 9 ns. These peak structures, however have a high noise proportion at an estimated pulse width of $\sim$ 500 ps. Detectable changes in these peak structures at other split potential configurations have not been found.

The ion spectra shown have no clear pulse, compared to the electron spectra. The measurements seem to be either largely polluted by noise or all pulse structure of the electrons has gone lost in the transfer to an argon pulse via ionization. A multitude of ion spectra varying all experimental parameters have been measured. Unfortunately this behaviour seem to be the trend across all ion measurements of the half-EBIS setup independent of any experimental parameters.

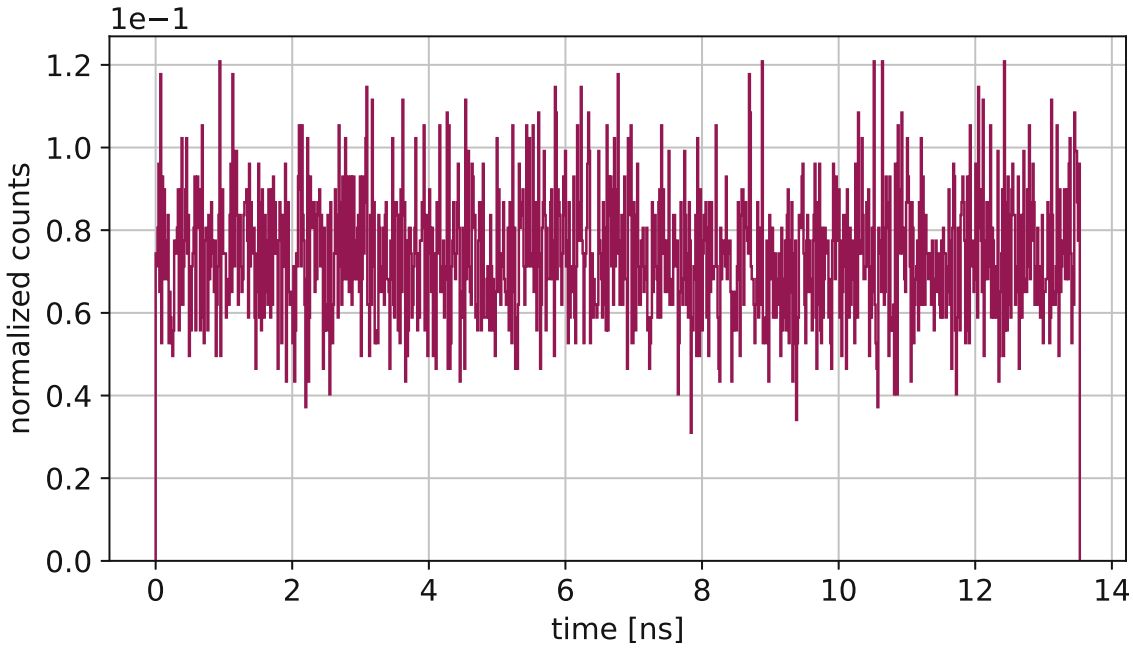

Figure 5.8.: Ion spectrum measured with potential configuration: V3 = −1 kV, V4 = 4 kV, V5 = V6 = 0 kV. The spectrum is very noise polluted. Any pulse information is lost.

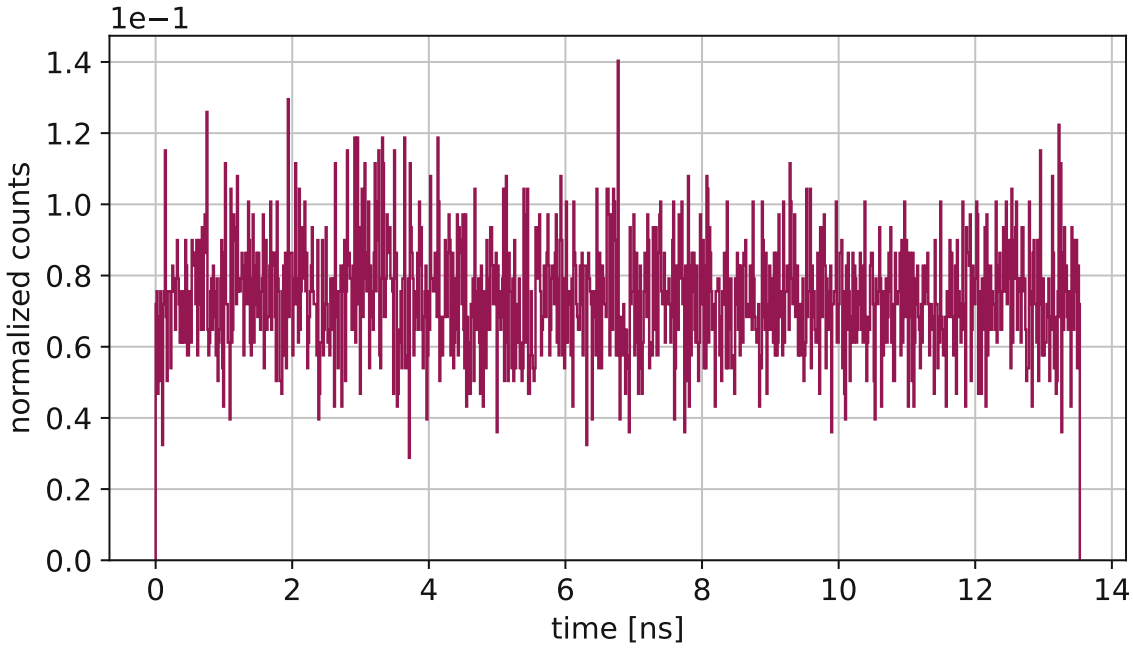

Figure 5.9.: Ion spectrum measured at lower gas pressure of $5 \cdot 10^{-6}$ mbar. The spectrum does not improve compared to Fig. 5.8.

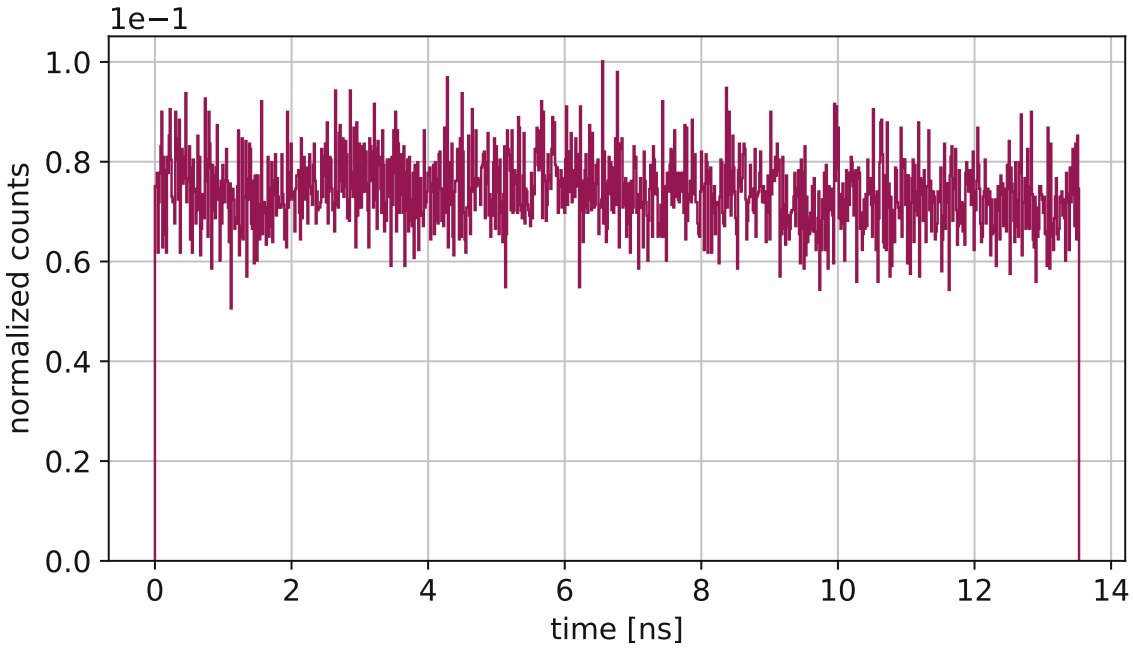

Figure 5.10.: Ion spectrum measured at lower cathode heating current of 200 mA. At low heating currents we have better electron pulse shapes which should translate to more clear ion pulses. The spectrum does not significantly improve compared to Fig. 5.9.

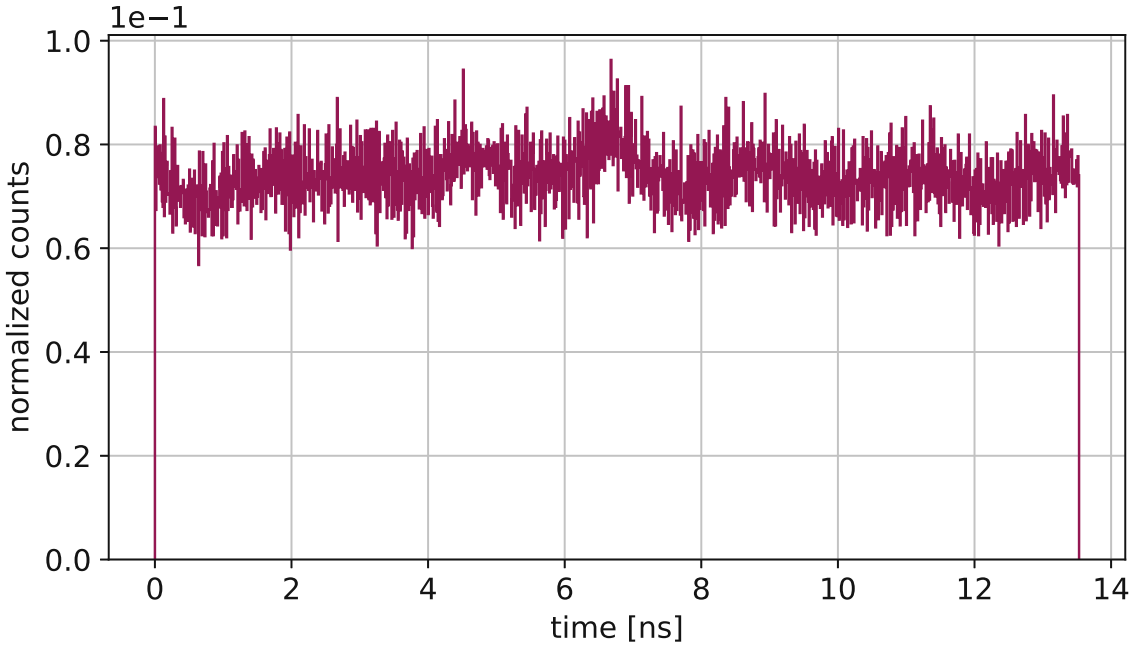

Figure 5.11.: Ion spectrum measured with potential configuration: V3 = −1 kV, V4 = 5 kV, V5 = 3 kV, V6 = 1 kV. The noise is more evenly uniform across the TOF interval, however pulse information is still lost.

The production of ion pulses is clearly more complicated than the production of electrons pulses. An ion pulse depends on more parameters of the setup than an electron pulse. The distinct advantage of electron pulse generation is the localized origin of electrons. Electrons are only directly extracted from the cathode. Placing a potential gradient right in the vicinity of the cathode ensures all electrons are accelerated to the same kinetic energy within a relatively small energy window upon their extraction. After extraction only space charge repulsion during flight time may broaden the electron pulse. However, during ion measurements the entire vacuum chamber is filled with argon. As such ion pulse generation via EII the ions may be created across the whole length of the electrons flight path, which may even extend past the EBIS volume depending on the electrode potential configuration. This means ion generation is not localized and in the half-EBIS setup argon may even be ionized outside the EBIS. Consequently since the potentials within the EBIS vary depending on the electrode build structure (electrode gaps, diameters, lengths) and the applied electrode potentials, ions are accelerated to a multitude of different kinetic energy ranges depending on their ionization point. This circumstance implies that an ion pulse generated by the an electron pulse is already inherently broadened upon ionization. Previous works conducting simulations of our setup suggest the creation of ions at higher and steeper potentials slope for optimal ion pulses with short pulse widths. In these simulations potential differences up to 10 kV over 1 mm were simulated. However, electrons gain a high amount of kinetic energy at such slopes which reduces their EII possibility since EII cross sections for singly ionized argon reduces by over a magnitude after the peak after about 80 eV [20]. Furthermore one can see a dependence on the argon gas pressure, which dictates the likelihood of collisions between electrons and argon atoms occurring.

5.1.2. Full-EBIS Measurements

The full-EBIS setup includes all electrodes (V3-V9) with surrounding magnets. The advantages/ disadvantages are inverted compared to the half-EBIS, as in the mirror has to be placed very close to the EBIS beam axis since the geometry of the collector electrode significantly reduces the opening angle. However, we can filter out electrons with full-EBIS thereby preventing EII outside of the EBIS. All spectra shown in this section are modulated with the laser repetition value.

Electrons

In Fig. 5.12 an electron TOF measurement of the full-EBIS setup is shown. The potential were set as follows: V3 = −0.2 kV, V4 = 0.05 kV, V5 = 0.1 kV, V6 = 0.2 kV, V8 = 0 kV, V7 and V9 are always grounded. Depending the on the potential setting of V3 and V8 the electrons can be trapped in the EBIS (V3 > V8) or we can let them

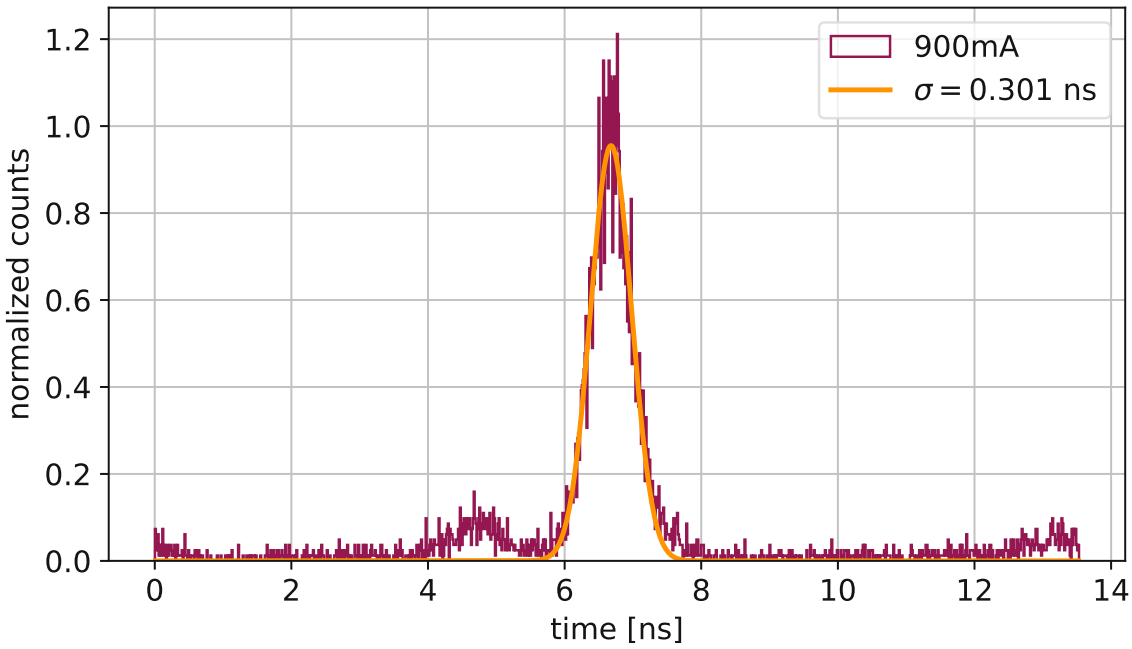

Figure 5.12.: Modulated electron spectrum taken with the full EBIS setup at the following potential settings: V3 = −0.2 kV, V4 = 0.05 kV, V5 = 0.1 kV, V6 = 0.2 kV, V8 = 0 kV. The cathode heating current was set at 900 mA. The resulting pulse width is calculated to be $2.3458 \cdot \sigma \approx 700$ ps.

exit the EBIS (V3 < V8). A new BaO cathode was installed for the full-EBIS setup. The combination of the new cathode and the full-EBIS only showed pulsed electron emission at higher cathode heating currents. In the measurement shown in Fig. 5.12 the heating current was set to 900 mA. The MCP was set to 0 kV/ 2 kV/ 2.2 kV (front, back, anode). Argon gas is removed for electron measurement, with a residual gas pressure of under 10^{-9} mbar subsisting. The measurement shows an electron pulse with a pulse width of $\sim$ 700 ps with a ptr of about 5. measured at a MCP count rate of 10 Hz.

Although it is not very relevant for electrons, the choice of these gradients was determined by the assumption that a high and steep potential slope is the optimal setting for ion pulse generation, as shown by simulations in previous works. The steepest slopes may be set between V4 and V5 or V6 and V7. The difference in these 2 gaps arises through the specific geometries of the electrodes (see Fig. 5.13). The first drift tube V4 has inner diameter of 3mm leading into the second drift tube V5 with a inner diameter of 5mm while the electrode separation distance is 1mm. This difference in diameters lets the potential of V4 reach rather deeply into the electrode volume of V5, which reduces the steepness of the slope itself. The third drift tube V6 has an inner diameter of 3

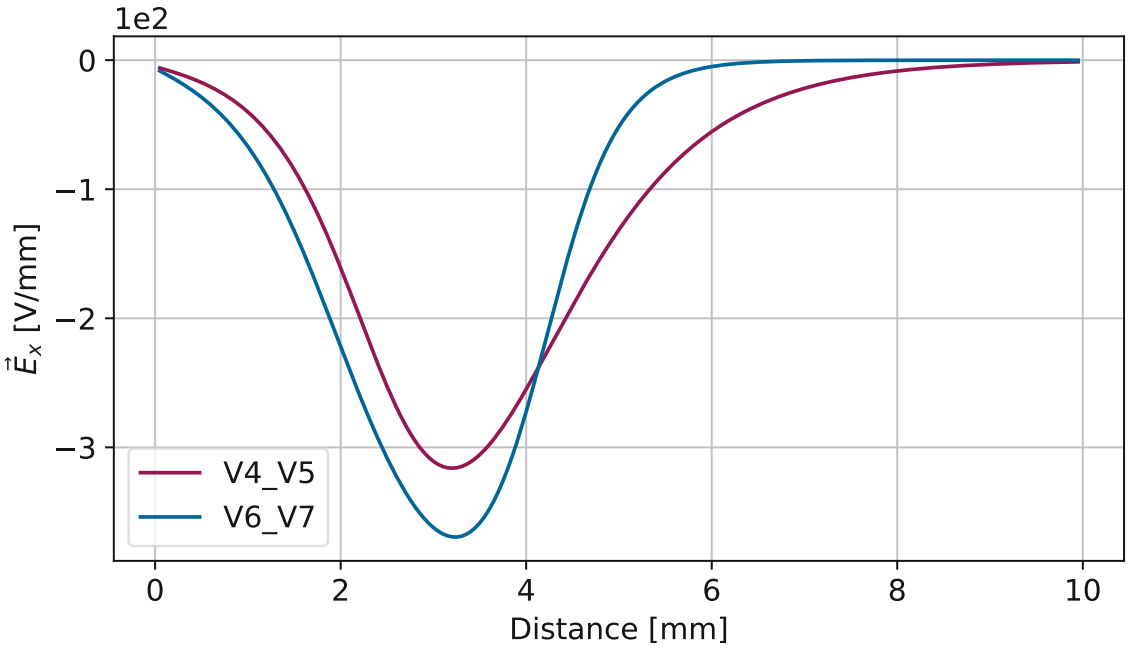

Figure 5.13.: Electric field in beam axis direction along the beam axis plotted once between drift tubes V4,V5 and once between drift tube V6 and collector V7. The absolute potential difference between V4,V5 and V6,V7 are equal. The field is stronger and sharper between V6,V7 than between V4,V5.

mm which leads to the collector V7 which has an inner diameter of 2 mm while the electrode separation distance is 2 mm. Although the electrode distance is higher than for V4, V5 the inner diameters are smaller which produces a steep slope. Overall the potential values were set low as to not induce too much kinetic energy into the electrons. Comparatively low energetic electrons are favourable for EII of argon since the EII argon cross section has a peak at $\sim$ 80 eV. This comes at a cost of not highly accelerating ions thereby having longer flight times during which an ion pulse may broaden. The potential configuration ideally only allows ions which are generated between V6 and V7 to exit the EBIS, since this is the only interval where we have positive gradient. The gradient between all other electrodes is negative and thereby accelerate ions away from the EBIS opening.

In Fig. 5.14 a similar measurement as in Fig. 5.12 was taken with the same gradient principle but with higher values. The potentials were set to V3 = −2 kV, V4 = 1 kV, V5 = 1.7 kV, V6 = 2 kV. All other parameters were left unchanged. The pulse width is $\approx$ 400 ps with a ptr of about 1. Comparing both spectra of Fig. 5.12 and Fig. 5.14, we see a reduction in pulse width at higher potential settings however proportionally the

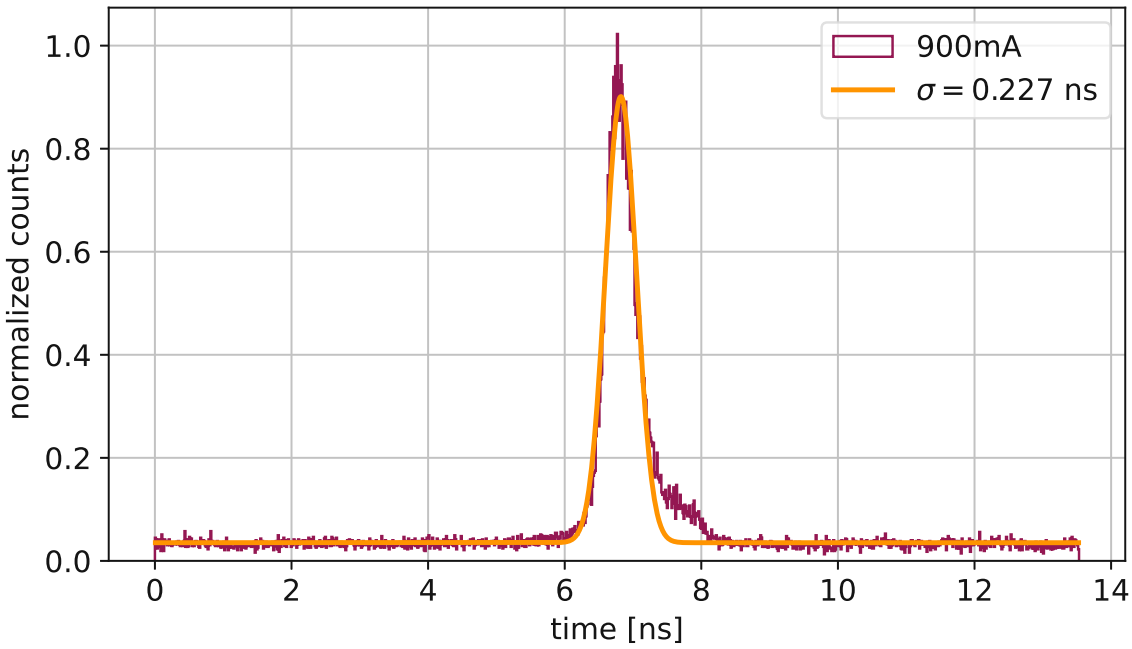

Figure 5.14.: Modulated electron spectrum taken with the full EBIS setup at the following potential settings: V3 = −2 kV, V4 = 1 kV, V5 = 1.7 kV, V6 = 2 kV. The cathode heating current was set at 900 mA. The resulting pulse width is calculated to be $2.3458 \cdot \sigma \approx 500$ ps.

ptr reduces significantly more. The reduction of pulse width is expected and understood however it is unclear how the higher potentials increases the noise/thermal level. One reason may be the that a higher negative cathode potential increase the probability latent thermal emission.

Ions

In Fig. 5.15 an ion TOF spectrum in shown. This spectrum was measured with the same potential configuration as used in the electron TOF measurement in Fig. 5.12. The MCP potentials were adjusted for ion measurements (-2 kV/ 0 kV/ 0.1 kV). An argon gas pressure of $5 \cdot 10^{-7}$ mbar was set. In this measurement the repeller (V8) potential was kept at 0 kV. This means electrons were able to exit the EBIS during this measurement. The spectrum shows a noise polluted but nonetheless periodic wave structure. This structure is not discernible in the pre-modulated raw TOF spectrum. One assumption for this multiple peaks structure could that every peak corresponds to a different ion species other than argon. Since a perfect vacuum is not achievable, a certain amount of residual gas always remains in the chamber. The atomic composition

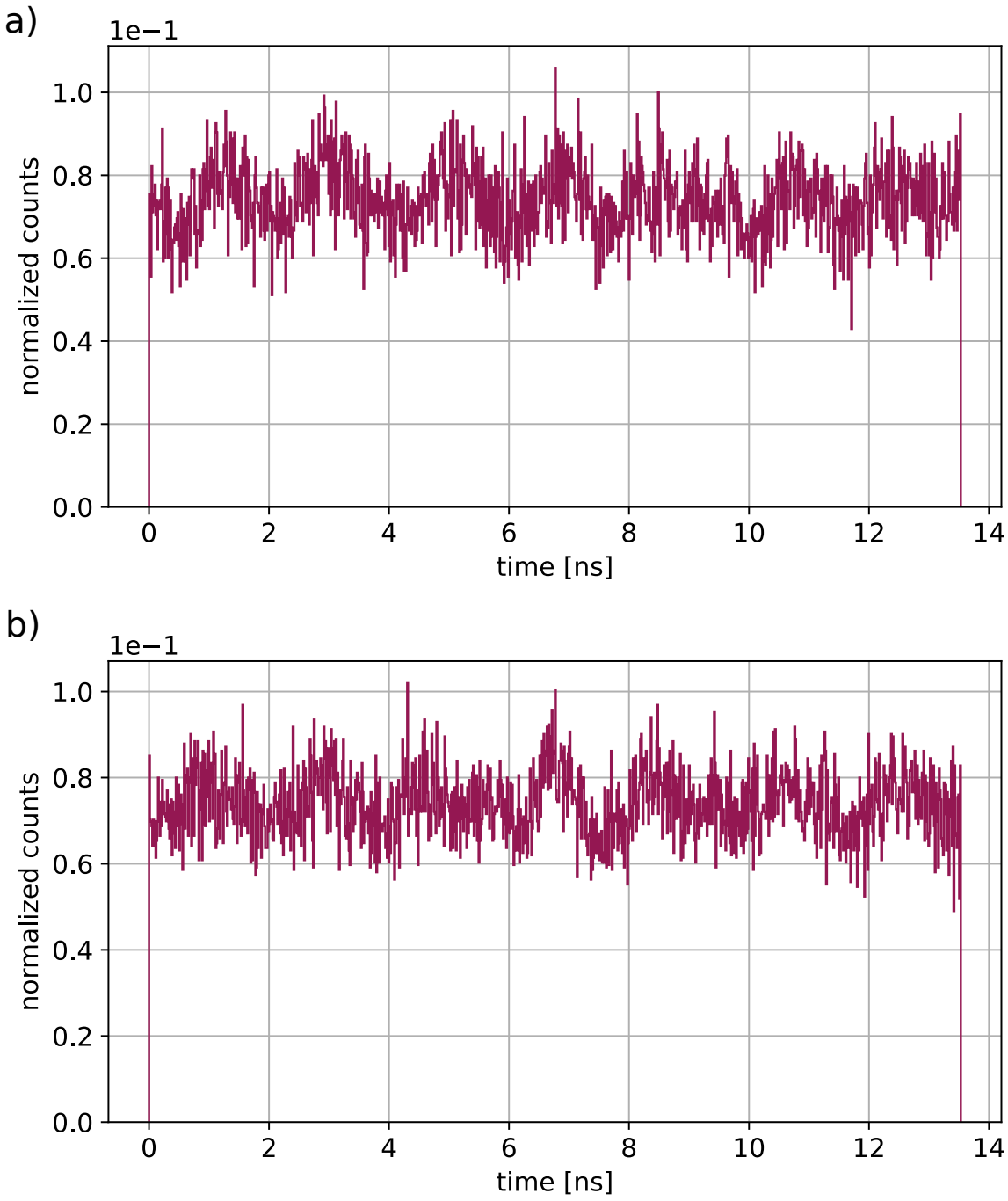

Figure 5.15.: a) Modulated ion spectrum take at potential settings: V3 = −0.2 kV, V4 = 0.05 kV, V5 = 0.1 kV, V6 = 0.2 kV, V8 = 0 kV. The argon gas pressure was set to $5 \cdot 10^{-7}$ mbar. It is difficult to extract information from the spectrum due to high noise level. However, a subtle wave structure with multiple peaks can be discerned. b) Modulated ion spectrum take at potential settings: V3 = −0.2 kV, V4 = 0.05 kV, V5 = 0.1 kV, V6 = 0.2 kV, V8 = −0.21 kV. The argon gas pressure was set to $5 \cdot 10^{-7}$ mbar. Improvements compared to the spectrum in a) are not significant. An ion pulse is not directly discernible in the spectrum.

of this residual gas most likely resembles the atomic composition of the atmosphere. Although we only fill our vacuum chamber with argon, we still have to account for the elements in the residual gas. This could significantly distort our spectrum, if certain gas species in the residual gas have a significantly larger EII cross section compared to argon and considering differing atomic masses leading to differing TOFs. The hypothesis of the peaks corresponding to different should be easily verifiable by conducting measurement at different argon pressures, which should to only change the height the peak corresponding to argon.

In Fig. 5.15 b) the same measurement was taken as in Fig. 5.15 a) with only one change in the experimental parameters. The repeller (V8) potential was lowered from 0 kV to -0.21 kV. This configuration has the repeller potential below the cathode potential, which means the electrons do not gain enough kinetic energy from the cathode potential to overcome the repeller potential. This setting traps the electrons within the inner volume of the EBIS, which ceases the possibility of EII outside the EBIS. This feature should ideally produce a cleaner TOF spectrum since stray ion created outside the EBIS cannot distort the measurement. However, when comparing the measured

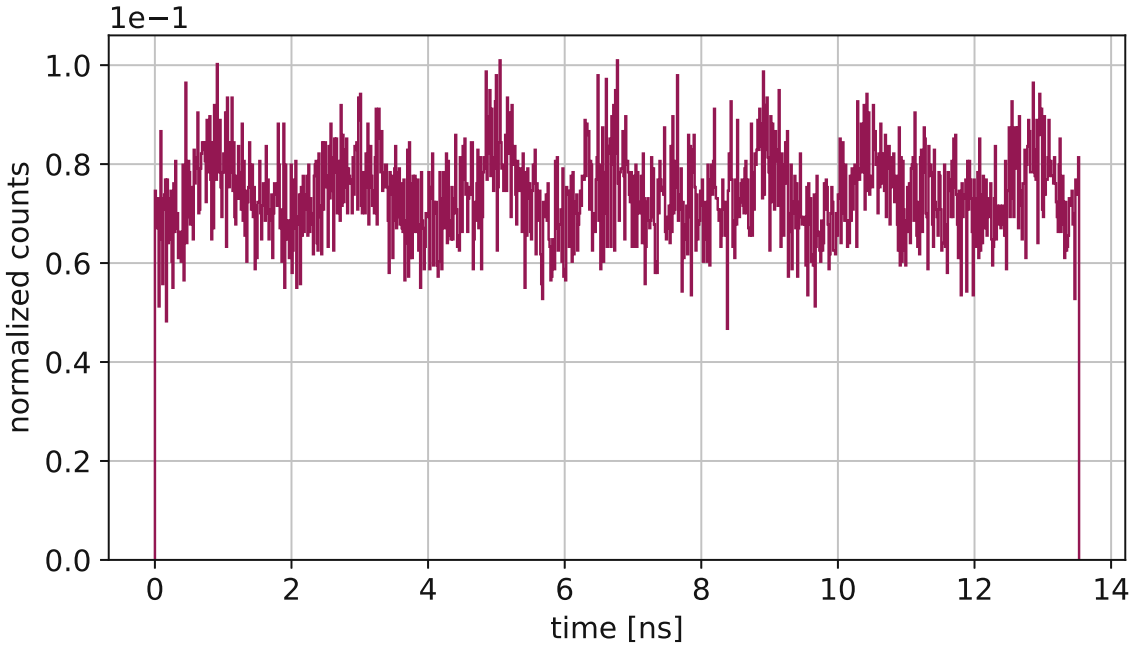

Figure 5.16.: Modulated ion spectrum take at potential settings: V3 = −2 kV, V4 = 1 kV, V5 = 1.7 kV, V6 = 2 kV, V8 = −3 kV. The slight wave structure in the ion spectrum remains even at high potential settings, however noise levels are still too high to discern a clear ion pulse.

spectra no clear difference other than the localized noise variations is discernible. This leads us to a conclusion that EII outside the EBIS may not be a significant contributor to pulse distortion.

In Fig. 5.16 an ion TOF measurement is shown, where the measurement is analogues to the electron TOF measurement of Fig. 5.14. These full-EBIS measurements were taken at high potentials. We again set the repeller (V8) potential to -3 kV significantly below the cathode (V3) potential at -2 kV. The argon pressure was set to 10^{-6} mbar. The spectra still shows us the periodic wave structure. However, changes compared to the spectra take at the low potential configuration are too difficult to discern.

Although the electron spectra shows clear changes between the low potential configuration and high potential configuration, the ion spectra are still too noise polluted for accurate analysis. The ion spectra shown here have been measured over several hours and up to 2.5 days. The average MCP count rate during the ion measurement is calculated to ca. 2 Hz. Pure noise measurements show noise levels of at-least 1Hz. As such we have at best 1 ion count for every noise count. Taking measurements at longer periods of time should ideally enable the ion counts to build upon themselves while the noise count distribute themselves across the whole timing interval. Additionally, since the electron pulses have a pulse width of ca. 500 ps, a conservative estimation would place a resulting ion pulse at at-least a few nanoseconds. A nanosecond pulse width combined with multiple gas species legible for EII (residual gas) and high noise levels is the assumed hypothesis that results in a distorted wave structure. Even longer measurements may shed more light on the data.

All the ion spectra shown have been argon ion spectra. During these measurements the argon pressure is always set to atleast 1 magnitude above the residual gas pressure at under 10^{-9} mbar. As such we have much more argon in our vacuum chamber compared to the amount of residual gas. However the peak in the spectra assumed to correspond to argon ions does not show a clear elevation compared to the other peaks assumed to correspond to the residual gas species. In an attempt to offset the possible inefficiencies of EII with argon we repeat measurements with nitrogen instead of argon and varying gas pressures. In Fig. 5.17 two ion TOF spectra are shown. The measurement was conducted first with a nitrogen gas pressure of 10^{-9} mbar and a second at 10^{-6} mbar pressure. The potential configuration was set as follows: V3 = -0.2 kV, V4 = 0.05 kV, V5 = 0.1 kV, V6 = 0.2 kV, and V8 = -0.21 kV. The BaO cathode was heated with a current a current of 900 mA. MCP was set to -1.98 kV/ 0 kV/ 0.1 kV. The spectra are still very polluted by noise and the periodic wave structure is visible. The differences in nitrogen pressure are not significantly visible in the spectra. The high noise levels show that the rate of ionization is still too low for a clear ion pulse to be discernible above the

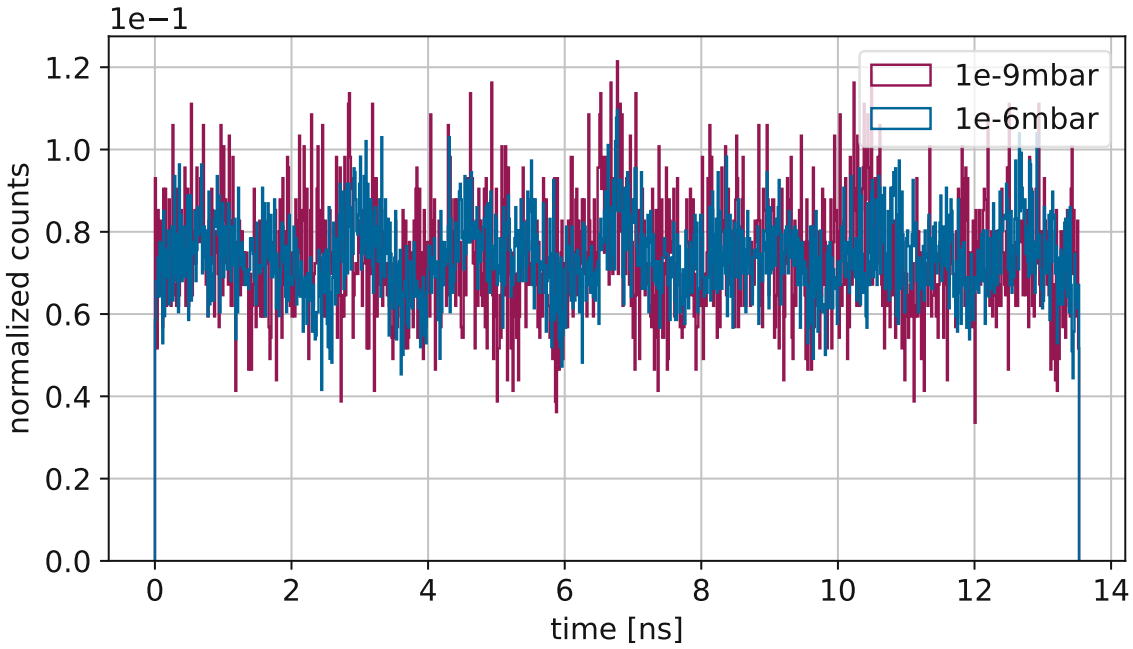

Figure 5.17.: Modulated TOF spectrum of nitrogen ions taken at potential settings: V3 = −0.2 kV, V4 = 0.05 kV, V5 = 0.1 kV, V6 = 0.2 kV, and V8 = −0.21 kV. Two spectra were recorded, once for a nitrogen gas pressure of 10^{-9} mbar and once at a pressure of 10^{-6} mbar. By switching the ion species from argon to nitrogen which has a lower first ionization energy (see Fig. 2.1) one should be able to create more ions. The spectrum unfortunately does not show much difference in noise levels, regardless of pressure levels. A slight wave structure subsists at both ion species.

noise. As the ionization rate among other factors depends directly on the pulse electron output current from the cathode and because this current still proves to be poor, further efforts put towards an improvement of this aspect of the experiment are recommended.

5.2. Simulation and Comparison

As mentioned in a previous chapter, we also simulate the experiment via ion trajectory simulator Simion. We simulate the experimental parameters of the results of full-EBIS measurements shown in this work. The simulations produce an idealistic results which are only difficult if not impossible to achieve in the experiment. Nonetheless the simulation provides useful insights towards the limiting case of results under perfect experimental conditions. Since we currently do not filter particles in regards to their energy,

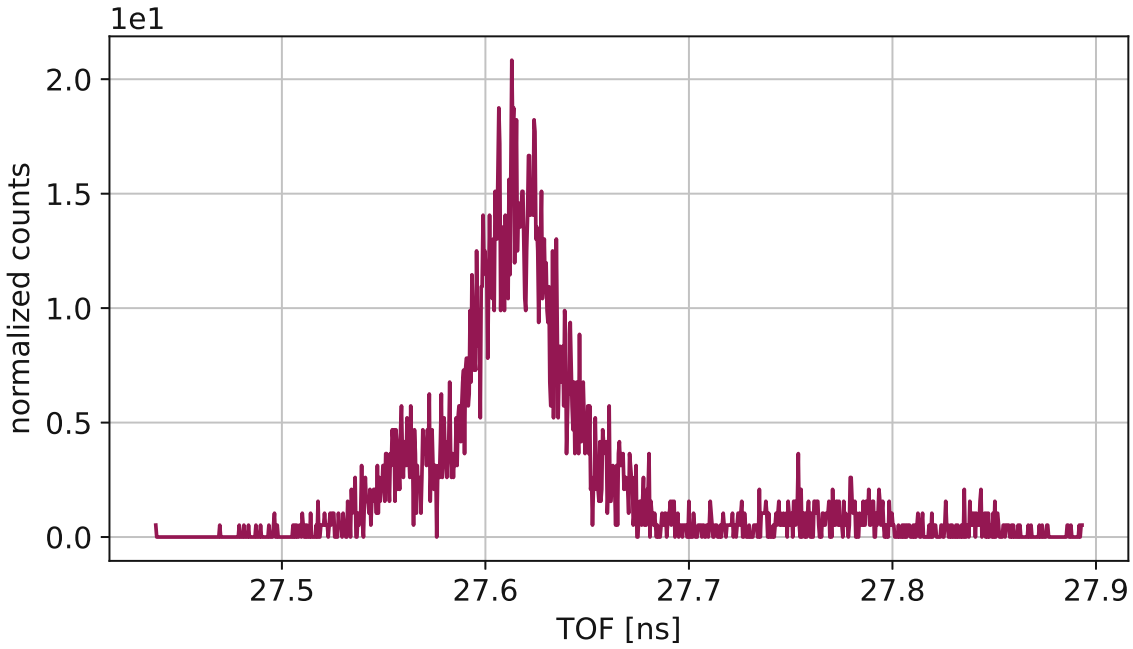

Figure 5.18.: Simulated electron spectrum at potentials V3 = −0.2 kV, V4 = 0.05 kV, V5 = 0.1 kV, V6 = 0.2 kV, V8 = 0 kV. The electrons arrive at the MCP from the cathode at a mean TOF of ca. 27.62 ns. The pulse width is calculated to be ca. 50 ps. The simulated spectrum shows a similar small TOF heap left of the main peak as in Fig. 5.12. The origin of this small peak is not easily explained since it does not show a simple direct dependency on any one aspect of the simulation (e.g. initial positions, initial velocity).

we also do not included energy filtering in the simulation.

Electrons

In Fig. 5.18 an simulated electron TOF spectrum is shown. The simulation was conducted at the following potential configuration: V3 = −0.2 kV, V4 = 0.05 kV, V5 = 0.1 kV, V6 = 0.2 kV, V8 = 0 kV, and as always V7=V9=0. The MCP front plate is set to 0 kV. Cathode heating currents, gas pressures, and the laser properties are not directly included in the simulation. This simulation is a direct analogue to the presented electron spectrum Fig. 5.12. Since Simion only simulates one particle at a time, space charge effects are not included. We need not modulate out simulated spectrum, as was required for the experimental results, since we can simulate all particles as part of a singular pulse and thus record their absolute TOFs. As can be seen in the spectrum the TOF mean lies around 27.62 ns. The pw of the simulated spectrum is ca. 50 ps. A

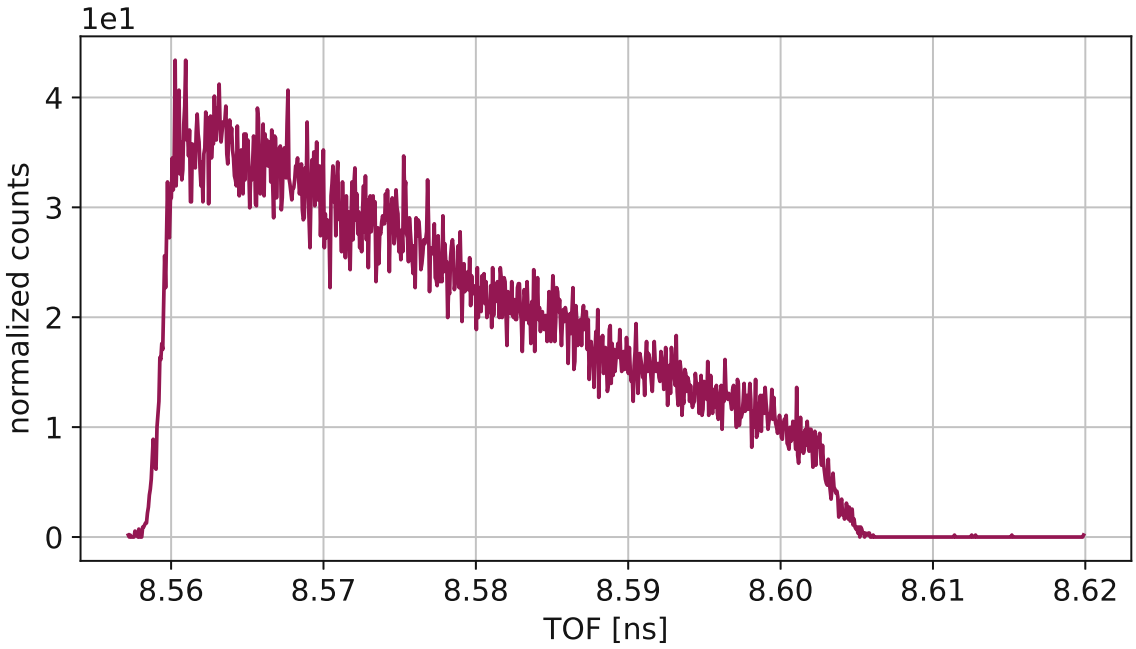

Figure 5.19.: Simulated electron spectrum at potentials V3 = −2 kV, V4 = 1 kV, V5 = 1.7 kV, V6 = 2 kV, and V8 = 0 kV. The electrons arrive at the MCP from the cathode at a mean TOF of ca. 8.57 ns. The pulse shape does not resemble a Gaussian anymore, as such a pulse width definition at full width at half maximum does not make much sense. One can estimate a pulse width as the difference in TOF of the leading edge and the tailing edge of the distribution. This approach gives a pulse width of ca. 40 ps.

considerable reduction from 500 ps of the experimental results. This hypothesis for this drastically higher pulse width in the experiment is most likely due to pulse broadening at the MCP due to its intrinsic detection method. An full concise investigation of this pulse broadening effect at the MCP is outside the scope of this work, and thus remains as a hypothesis in this thesis. Another interesting property shown by the simulation is that only 5% of the simulated electrons manage to reach the MCP. Only these 5% are included in Fig. 5.18. The other 95% collide with some other part of the setup. It seems that the choice of low potential values for the EBIS is not sufficient for efficient electron yield outside the EBIS. This means for full-EBIS setup only about 5% of the electrons are measured at the MCP. The percentage of measured electrons should be higher for the half-EBIS setup since it has a larger exit opening than the full EBIS setup.

In Fig. 5.19 we simulated analogue to the electron spectrum of Fig. 5.14. In case the following potentials were set: V3 = −2 kV, V4 = 1 kV, V5 = 1.7 kV, V6 = 2 kV,

and V8 = 0 kV. In this simulation we get an mean TOF of ca. 8.57 ns. Unfortunately at high potentials the pulse shape gets distorted in a way where a gaussian fit is not accurate anymore. Taking the difference of the leading and tailing edge of the distribution we approximate a pulse width of ca. 40 ps. Again magnitudes smaller than in the experiment. Another significant improvement of the high potential simulation over the low potential simulation of Fig. 5.18 is the electron yield at the MCP. With the high potentials close to 90% of electrons reach the MCP.

Ions

In Fig. 5.20 a simulated argon ion TOF spectrum is shown. The potentials were set to: V3 = −0.2 kV, V4 = 0.05 kV, V5 = 0.1 kV, V6 = 0.2 kV, V8 = 0 kV. The MCP front plate is set to -2 kV. This is the simulated analogue to the ion spectrum shown

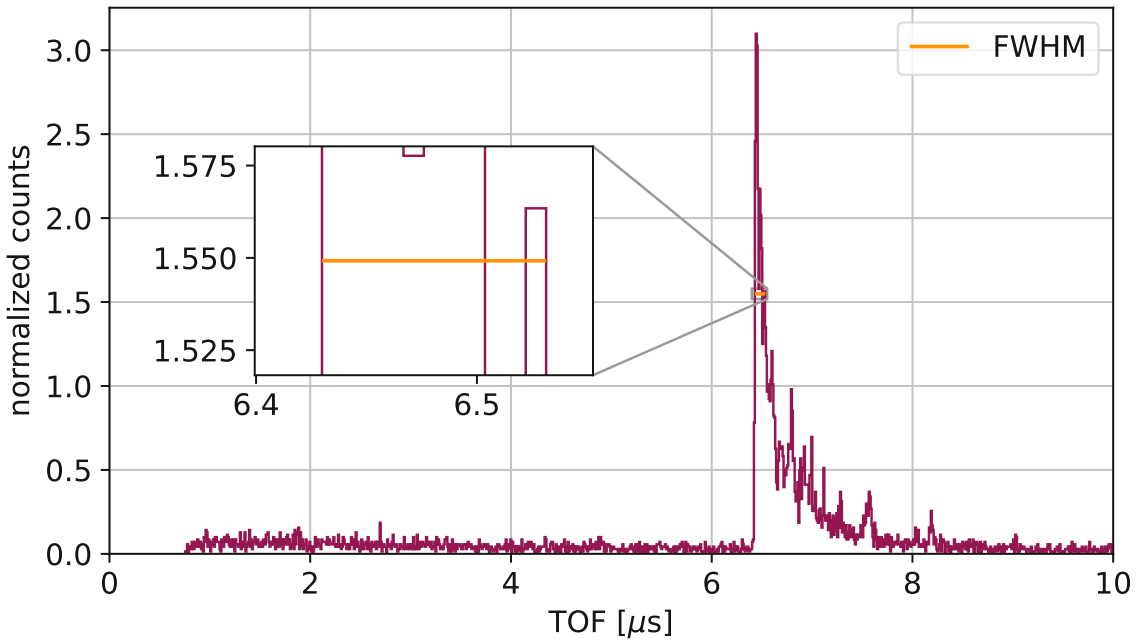

Figure 5.20.: Simulated argon ion spectrum recorded at potential settings: V3 = −0.2 kV, V4 = 0.05 kV, V5 = 0.1 kV, V6 = 0.2 kV, V8 = 0 kV. The spectrum shows a low noise level across the time interval due to ionization occurring outside the EBIS. A clear pulse peak can be seen in the spectrum at a TOF of ca. 6.5 μs. The pulse shape does not resemble a Gaussian. Still taking the full width at maximum as the pusle width is estimated to be in the low 100 nanosecond range.

in Fig. 5.15. We have a TOF peak at around ca. 6.5 μs. The data is cut off for the ions with TOFs over 10 μs. The pulse shape does not suit a gaussian fit. Nonetheless we can estimate a pulse width from Fig. 5.20 to be in the low 100 nanosecond range. The ion yield is ca. 10%. This means 10% of ion created in the simulation manage to reach the MCP. Furthermore, we configured the simulation such that ionization only occurs on negative potential gradients in beam line direction. These are the gradients that accelerate ion forwards out of the EBIS. All positive potential gradients accelerate ions backwards and are thus not of interest to us. The spectrum shows a small degree of noise across the TOF interval. This mostly arises from the choice of setting the repeller potential V8 to zero. This setting, as mention previously, allows electrons to exit the EBIS. This leads to ionization outside EBIS. These ions create the noise level seen at the TOF values below the TOF peak. In the next simulated spectrum shown in Fig. 5.21 where I lowered V8 to -0.21 kV. Now it is below the cathode potential

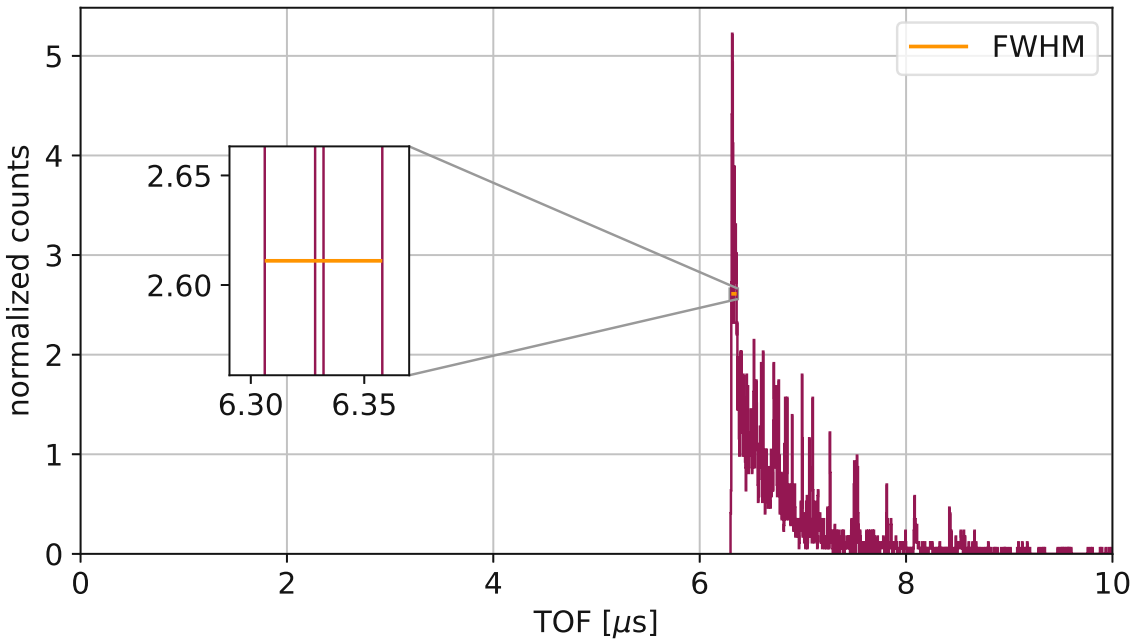

Figure 5.21.: Simulated argon ion spectrum recorded at potential settings: V3 = −0.2 kV, V4 = 0.05 kV, V5 = 0.1 kV, V6 = 0.2 kV, V8 = −0.21 kV. The spectrum shows considerably less noise across the time interval compare to Fig. 5.20. This is due to the fact that V8 is lower than V3. In this configuration electrons cannot exit the EBIS preventing ionization outside the EBIS reducing noise. The pulse width is estimated to in the mid 10 nanosecond range when compared to the pulse width estimation in Fig. 5.20

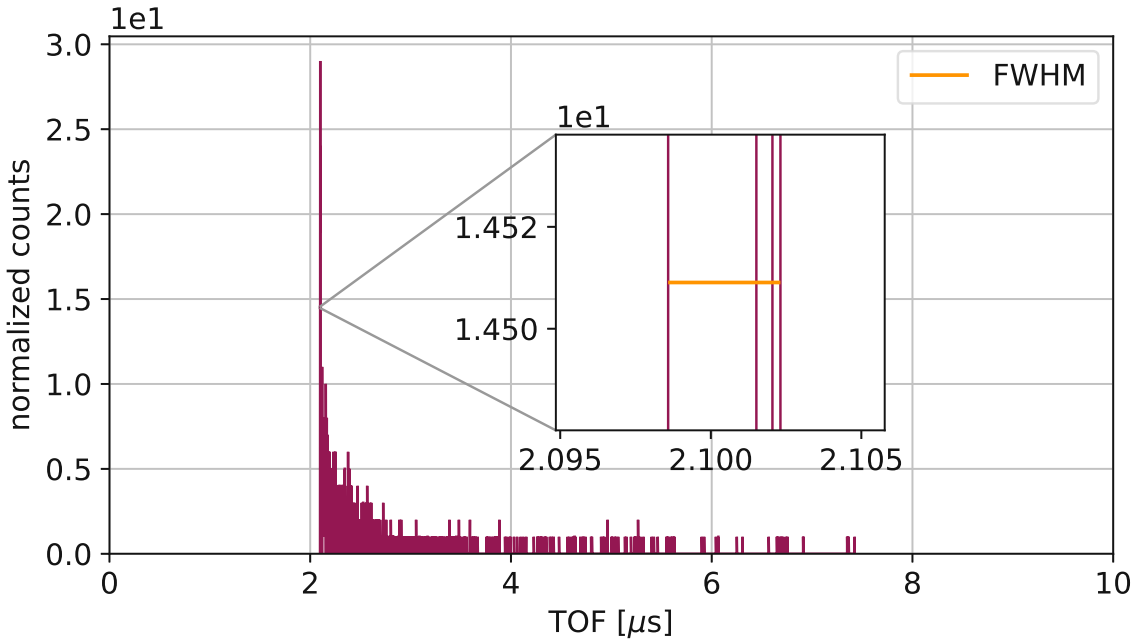

Figure 5.22.: Simulated argon ion spectrum recorded at potential settings: V3 = −2 kV, V4 = 1 kV, V5 = 1.7 kV, V6 = 2 kV, and V8 = −3 kV. The TOF peak is found at approx. 2.1 μs. The TOF distribution does not resemble a Gaussian distribution and features a long tail towards higher TOFs. The pulse however is more significantly higher and has a sharper fall off than the pulse in Fig. 5.21 (compared peaks). Based on this the pulse width is estimated to be a magnitude lower putting it in mid nanosecond range.

V3. This configuration traps electron within the EBIS and in the simulation electrons can oscillate between the cathode and repeller multiple times. Comparing Fig. 5.21 to Fig. 5.20 we see a clear reduction of the noise level before the TOF peak at around ca. 6.5 μs due to electron confinement. In regard the simulation suggests the confinement of electron, which is not possible with the half-EBIS setup. The ion yield with electron confinement is slightly reduced to 7%. This decrease is the result of the negative repeller potential attracting a few ions to itself, preventing them from reaching the MCP.

In Fig. 5.22 our final simulated ion spectrum is shown. This spectrum was recorded for high potentials in analogue to Fig. 5.16. As a reminder: V3 = −2 kV, V4 = 1 kV, V5 = 1.7 kV, V6 = 2 kV, and V8 = −3 kV. The spectrum shows a TOF peak at around 2.1 μs. An pulse width estimation is difficult to make since the distribution is not well fit by a gaussian, however it is safe to say that pulse width at the high potential gradient is lower than at the low potential configuration. The ion yield is slightly better at ca. 8%. The low potential configuration however has the benefit of producing lower energetic

electrons, which reflects itself in the EII cross section. The high potential configuration required the ten-fold amount of electrons to produced roughly the same number of ions as the low potential configuration did. Since the pulsed electron emission current from the cathode in the experiment is still relatively low, the low potential configuration is still advised over the high potential configuration for maximum EII efficiency despite seemingly worse pulse widths.

In Fig. 5.23 an energy filtered pulse width evaluation for the data of Fig. 5.22 is shown. The relative energy window was set to 10^{-4}. Only pulse widths with a standard deviation of below 10 ps are plotted. Pulse widths in the range of 100 ps are achievable in the simulated data. The energy values indicate that ions created close to the top of the potential slope between V6 and V7 provide the shortest pule widths.

Overall the simulations show that a pulse width determination for ions is difficult, since the overall TOF distribution shape does not correspond to a Gaussian distribution. Filtering the ions by their kinetic energy in relatively small energy windows seems to be a must do for experiment and simulation. Previous simulation works show that with energy filtering, the TOF distributions within an energy window more closely resembles a Gaussian distribution.

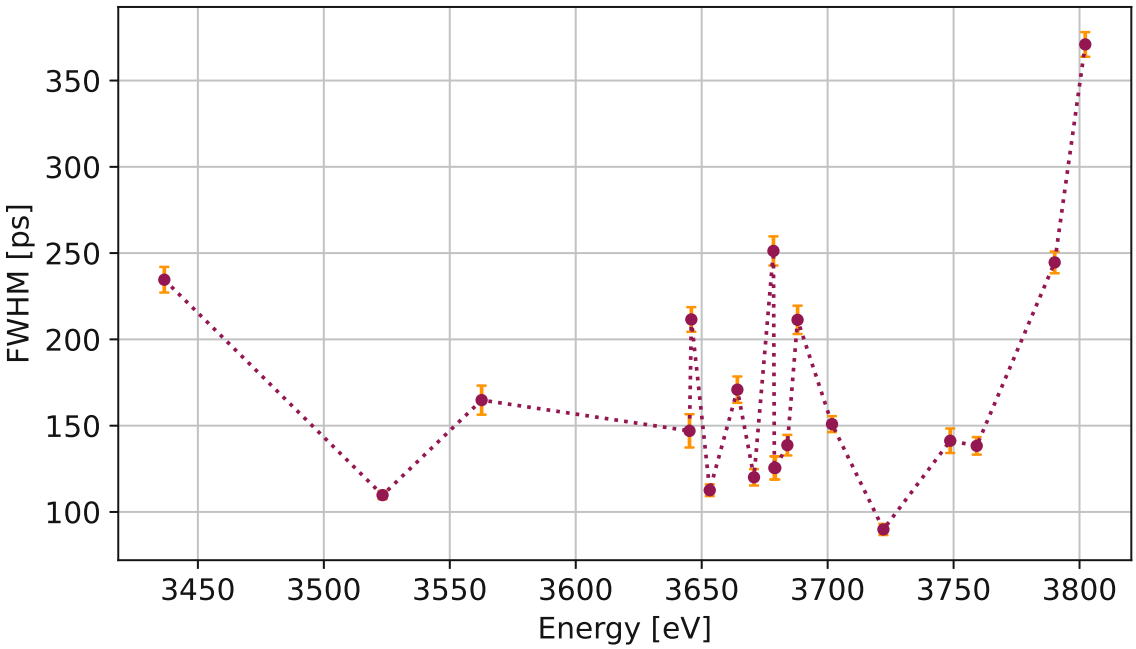

Figure 5.23.: Energy filtered pulse width (FWHM) evaluation for spectrum Fig. 5.22. The relative energy window is 10^{-4}. Only pulse widths with a standard deviation of below 10 ps are plotted.

6. Conclusion

We have designed an experimental setup intended to create ion pulses in a novel way for future pump/probe experiments. We utilize a femtosecond laser which is directed onto a BaO cathode to trigger emission of pulsed photo-electrons within an electron beam ion source (EBIS). The emitted pulsed photo-electrons interact with low pressure gas in a vacuum chamber via EII to create a ion pulse. The ion pulse is subsequently accelerated within the electron beam ion source which emits a pulsed ion beam. We measure the time of flight TOF of the pulse and determine the pulse width via the measured TOF distribution. The focus of this thesis was put on the generation of ion pulses and the optimisation of the ion pulse widths.

The EBIS is a small compact assembly of electrodes covering the cathode from nearly the full solid angle, as such we have had to direct our laser into the electron source to the cathode through the only available open solid angle given by the opening exit of said electron source. This setup constricts the possible positioning of the laser optics element used to redirect the laser to close proximity to the electron source beam axis, potentially blocking a fraction of our ion/electron beam. We have run the experiment in two variations of the electron source assembly which have different implications on the constriction of the optics element placement. The first variation is the half-EBIS operation. The half-EBIS operation has a larger opening solid angle to the cathode. This gives us more freedom in the optics element placement, however this comes at the cost of losing the ability to filter out the electrons. Not being able to filter electrons may induce ionization outside the EBIS. These ions have no time structure and as such may distort our ion pulse during measurements. With the half-EBIS operation we have managed to create electron pulses down to $\approx$ 500 ps in pulse width, but we were not able to detect any ion pulses. The second variation of the setup is the full-EBIS operation, with which we can prevent electrons from exiting the EBIS at the cost of more lower tolerances for the optics element placement. In the full-EBIS operation we have also managed to create electron pulses down to about $\approx$ 500 ps in pulse width. The generation of ion pulses still remains difficult even in full-EBIS operation. However, in the full-EBIS operation we do notice a temporal structure in the ion spectrum with a direct relation to the femtosecond laser repetition rate.

There are multiple hypothesis as to why we see no clear ion pulses. Pulsed photo-

electron measurements in half-EBIS operation show that the pulsed photo-electron current induce by the femtolaser pulse is only about 1 electron for every 10 laser pulses. This pulse photo-electron current is assumed to be too low for effective generation of sufficient ions to produce a detectable ion pulse. Another hypothesis is the delocalized ionisation volume. The electrons can in principle ionize anywhere within the EBIS which gives a high kinetic energy spread of the ions, this can lead to considerable pulse broadening. For effective ion pulse production ionization has to ideally be localized to a small volume. The last hypothesis is that we do generate ion pulses, however the pulse widths are significantly larger than the femtolaser repetition rate. In this scenario ion pulses are created at such high frequencies that they overlap each other significantly before they can be measured, leading to a near uniform ion TOF distributions as shown in Subsec. 5.1.1.

In parallel to conducting the experiment I have also setup a realistic simulation which allows us to test certain experimental conditions more freely. The simulation is an improvement previous works done by myself and the time4ions group. The simulation includes trajectory simulations of electrons as well as argon (ions). A virtual EII collision process is coded into the simulation with which the electrons may create ions. The EII collision is dependent on the argon EII cross section approximation proposed by Peterson and Allen [21]. The simulation shows that an electron pulse in the 10 ps region to be ideally achievable. Ion pulse widths are difficult to determine since their TOF distribution does not resemble a Gaussian nor does it have two clear edges. However based on the microsecond TOFs of the ions, I estimate the pulse width by considering the full width at half maximum of the peak structure to be in the 10 to 100 ns region.

References

(1) Qader, N.; Kök, M.; Dagdelen, F.; Aydoğdu, Y. A review of smart materials: researches and applications. *El-Cezeri* **2019**, *6*, 755 –788.

(2) Kozubek, R.; Tripathi, M.; Ghorbani-Asl, M.; Kretschmer, S.; Madauß, L.; Pollmann, E.; O'Brien, M.; McEvoy, N.; Ludacka, U.; Susi, T.; Duesberg, G. S.; Wilhelm, R. A.; Krasheninnikov, A. V.; Kotakoski, J.; Schleberger, M. Perforating Freestanding Molybdenum Disulfide Monolayers with Highly Charged Ions. *The Journal of Physical Chemistry Letters* **2019**, *10*, 904–910.

(3) Schwestka, J.; Inani, H.; Tripathi, M.; Niggas, A.; McEvoy, N.; Libisch, F.; Aumayr, F.; Kotakoski, J.; Wilhelm, R. A. Atomic-Scale Carving of Nanopores into a van der Waals Heterostructure with Slow Highly Charged Ions. *ACS Nano* **2020**, *14*, 10536–10543.

(4) Wilhelm, R. A.; El-Said, A. S.; Krok, F.; Heller, R.; Gruber, E.; Aumayr, F.; Facsko, S. Highly charged ion induced nanostructures at surfaces by strong electronic excitations. *Progress in Surface Science* **2015**, *90*, 377–395.

(5) Ritter, R.; Wilhelm, R. A.; Stöger-Pollach, M.; Heller, R.; Mücklich, A.; Werner, U.; Vieker, H.; Beyer, A.; Facsko, S.; Gölzhäuser, A.; Aumayr, F. Fabrication of nanopores in 1 nm thick carbon nanomembranes with slow highly charged ions. *Applied Physics Letters* **2013**, *102*, 063112.

(6) Ghorbani-Asl, M.; Kretschmer, S.; Krasheninnikov, A. V. Two-dimensional materials under ion irradiation: from defect production to structure and property engineering. *Materials Today* **2022**, 259–301.

(7) Charbonneau, S.; Poole, P. J.; Feng, Y.; Aers, G. C.; Dion, M.; Davies, M.; Goldberg, R. D.; Mitchell, I. V. Band-gap tuning of InGaAs/InGaAsP/InP laser using high energy ion implantation. *Applied Physics Letters* **1995**, *67*, 2954–2956.

(8) Nebogatikova, N. A.; Antonova, I. V.; Erohin, S. V.; Kvashnin, D. G.; Olejniczak, A.; Volodin, V. A.; Skuratov, A. V.; Krasheninnikov, A. V.; Sorokin, P. B.; Chernozatonskii, L. A. Nanostructuring few-layer graphene films with swift heavy ions for electronic application: tuning of electronic and transport properties. *Nanoscale* **2018**, *10*, 14499–14509.

(9) Zewail, A. H. Laser Femtochemistry. *Science* **1988**, *242*, 1645–1653.

(10) Golombek, A.; Breuer, L.; Danzig, L.; Kucharczyk, P.; Schleberger, M.; Sokolowski-Tinten, K.; Wucher, A. Generation of ultrashort keV Ar+ ion pulses via femtosecond laser photoionization. *New Journal of Physics* **2021**, *23*, 033023.

(11) Breuers, A.; Herder, M.; Kucharczyk, P.; Schleberger, M.; Sokolowski-Tinten, K.; Wucher, A. A concept to generate ultrashort ion pulses for pump-probe experiments in the keV energy range. *New Journal of Physics* **2019**, *21*, 053017.

(12) Fries, J. Design of an electron beam ion source for experiments with ultrafast timing resolution using SIMION simulations, IAP, Technische Universität Wien, 2020.

(13) First Ionization Energy blocks.svg, `https://commons.wikimedia.org/wiki/File:First_Ionization_Energy_blocks.svg`, Last opened: 2022-21-11.

(14) Rapp, D.; Englander-Golden, P. Total Cross Sections for Ionization and Attachment in Gases by Electron Impact. I. Positive Ionization. *The Journal of Chemical Physics* **1965**, *43*, 1464–1479.

(15) Ehrhardt, H.; Hesselbacher, K. H.; Jung, K.; Schulz, M.; Tekaat, T.; Willmann, K. Measurements of double differential cross sections in electron impact ionization of helium and argon. *Zeitschrift für Physik A Hadrons and nuclei* **1971**, *244*, 254–267.

(16) Crowe, A.; Preston, J. A.; McConkey, J. W. Ionization of Argon by Electron Impact. *The Journal of Chemical Physics* **1972**, *57*, 1620–1625.

(17) De Heer, F. J.; Jansen, R. H. J.; van der Kaay, W Total cross sections for electron scattering by Ne, Ar, Kr and Xe. *Journal of Physics B: Atomic and Molecular Physics* **1979**, *12*, 979.

(18) Hayashi, M. Bibliography of Electron and Photon Cross Sections with Atoms and Molecules Published in the 20th Century - Argon -, NIFS-DATA-072, 2003.

(19) Yanguas-Gil, A.; Cotrino, J; Alves, L. L. An update of argon inelastic cross sections for plasma discharges. *Journal of Physics D: Applied Physics* **2005**, *38*, 1588.

(20) Bretagne, J; Callede, G; Legentil, M; Puech, V Relativistic electron-beam-produced plasmas. I. Collision cross sections and loss function in argon. *Journal of Physics D: Applied Physics* **1986**, *19*, 761.

(21) Peterson, L. R.; Allen, J. E. Electron Impact Cross Sections for Argon. *The Journal of Chemical Physics* **1972**, *56*, 6068–6076.

(22) McConkey, J. W.; Crowe, A.; Hender, M. A. Differential Cross Sections in the Electron Impact Ionization of Atoms and Molecules. *Phys. Rev. Lett.* **1972**, *29*, 1–4.

(23) Johnson, A. S.; Avni, T.; Larsen, E. W.; Austin, D. R.; Marangos, J. P. Attosecond soft X-ray high harmonic generation. *Philos. Trans. A Math. Phys. Eng. Sci.* **2019**, *377*, 20170468.

(24) Constant fraction 1.svg, `https://commons.wikimedia.org/wiki/File:Constant_fraction_1.svg`, Last opened: 2022-21-11.

(25) Simion Software Package, `https://simion.com/download`, Last opened: 2022-11-10.

(26) Grossek, A. Ion trajectory simulations for the determination of a lower pulse width bound for a fast pulsed EBIS, IAP, Technische Universität Wien, 2021.

(27) User Programming, `https://simion.com/info/index.html`, Last opened: 2022-11-10.

(28) Simion User Forums, `https://forum.simion.com/topic/2797-user-program-splat-recording-not-working-properly/`, Last opened: 2022-10-11.

A. Documentation User Program

The Simion user program (SUP) feature is used in the Simion workbench for advanced ion trajectory simulations which cannot be done through Simion graphical user interface (GUI). In general, it is advised to use the SUP for simulations since it allows much more customization options than the GUI. The SUP is coded in the Lua programming language. In the following the Simion user program is documented in full detail:

In Fig. A.1 code lines 1 to 31 are shown. In line 1 the SUP is initialized. This command is inserted automatically by Simion upon SUP creation through the GUI. In line 3 I define a conversion variable which converts velocities from $\frac{\text{mm}}{\mu\text{s}}$ units to atomic units ($\hbar = e = m_e = a_0 = 1$) and vice versa. This variable is needed because Simion uses a mix of unit systems, whereas I calculate values in atomic units. Line 5 loads in the "particlelib.lua" software module into the variable "PL". This file can be found in the Simion installation/examples folder. This file enables us to interface the fly2 files through the SUP which loads the particles with varying initial conditions into the simulation. This is especially helpful for automation of multiple simulation runs. Without the "particlelib.lua" file, one would have to edit particle initial conditions in the fly2 files directly. In line 6 the temperature of the particles is set. This is required because a few initial conditions of the particles are defined by the Maxwell-Boltzmann velocity distribution. On line 9 a variable "last_write" is created. This variable is used later in the SUP to prevent double recording of particle initial/final conditions. On line 10 an array "child_ions" is initialized. In this array the ionization points of the argon induced by virtual electron impact are recorded, which is used to initialize the ions for ion simulations.

In line 13 the function "segment.flym" is defined. This function is required in the SUP as it is used to set the configuration for simulation runs. This function is called once one starts the simulation via clicking the "Fly'm" button in the GUI. The lines after line 13 are indented, to indicated that these lines are within the "segment.flym" function. Lines 14 and 15 are comments. In Lua all lines starting with double minus define comments. Lines [17, 30] sets the configuration for an electron simulation. In line 17 the number of electrons to be simulated is set. In line 17 the MCP potential in volt is set. In line 16 the cathode (=Vcat=V3), the drift tubes (V4 to V6), and the repeller (=Vrep=V8) potentials are set respectively. Lines [21, 23] creates a file with the "io.open" function

```
1  simion.workbench_program()
2
3  local convert_au_to_mmus = 2187.691264
4
5  local PL = simion.import './particlelib.lua'
6  local T=3e2 --Particles Temperature
7
8
9  local last_write=0
10 local child_ions = {}
11
12
13 function segment.flym()
14 ------------------------------------------------
15   --simulation electron measurement
16
17   N_e=1e5
18   Vmcp=0e3
19   Vcat, V4, V5, V6, Vrep = -0.2e3, 0.05e3, 0.1e3, 0.2e3, 0e3
20
21   spec = io.open("ele_" .. tostring(Vcat) .. "_" .. tostring(V4) .. "_" ..
22                  tostring(V5) .. "_" .. tostring(V6) .. "_" .. tostring(Vrep)
23                  .. ".txt", "w")
24   spec:write("--ion_number, ion_charge, ion_time_of_flight[us], ion_px_mm[mm],
25               ion_py_mm[mm], ion_pz_mm[mm], ion_vx_mm[mm/us], ion_vy_mm[mm/us],
26               ion_vz_mm[mm/us], E_kin[eV] \n")
27
28   PL.reload_fly2('./elektron.fly2', {N_e=N_e, T=T})
29   run()
30   spec:close()
31
```

Figure A.1.: Simion User Program Lines [1, 31]

where the electron final conditions are recorded. "io.open" takes 2 arguments. The first argument is the file name, in this case "ele" (short for electron spectrum) followed by the EBIS potential separated by underscore signs. The second argument sets the file rights. In this case "w" for write rights. The file is accessible through the "spec" variable. In lines [24, 26] we label the file with a header, indicating the format in which the final conditions are recorded. In line 28 the "reload_fly2" function of the "particlelib.lua" software module is called via "PL" (see line 5). "reload_fly2" takes 2 arguments. The first is the fly2 file used to initialize particles. In this case "elektron.fly2" for electrons.

The second argument is the an array containing the number of particles and temperature variables are passed on to the fly2 file for particle initialization. In line 29 the electron simulation is started by the "run" command. This command executes all other functions in the SUP. Once the electron simulation has concluded line 30 is executed. This line closes the file in which in particle final conditions are recorded.

```
32  ------------------------------------------------------------
33    --simulation ion measurement
34    child_ions={}
35
36    --electrons
37    N_e=1e2
38    Vmcp=-2e3
39    Vcat, V4, V5, V6, Vrep = -0.2e3, 0.05e3, 0.1e3, 0.2e3, 0e3
40
41    spec = io.open("ionele_" .. tostring(Vcat) .. "_" .. tostring(V4) .. "_" ..
42                   tostring(V5) .. "_" .. tostring(V6) .. "_" .. tostring(Vrep)
43                   .. ".txt", "w")
44    spec:write("--ion_number, ion_charge, ion_time_of_flight[us], ion_px_mm[mm],
45                ion_py_mm[mm], ion_pz_mm[mm], ion_vx_mm[mm/us], ion_vy_mm[mm/us],
46                ion_vz_mm[mm/us], E_kin[eV] \n")
47
48    PL.reload_fly2('./elektron.fly2', {N_e=N_e, T=T})
49    run()
50    spec:close()
51
52    --ions
53    spec = io.open("ion_" .. tostring(Vcat) .. "_" .. tostring(V4) .. "_" ..
54                   tostring(V5) .. "_" .. tostring(V6) .. "_" .. tostring(Vrep)
55                   .. ".txt", "w")
56    spec:write("--ion_number, ion_charge, ion_time_of_flight[us], ion_px_mm[mm],
57                ion_py_mm[mm], ion_pz_mm[mm], ion_vx_mm[mm/us], ion_vy_mm[mm/us],
58                ion_vz_mm[mm/us], E_kin[eV] \n")
59
60    assert(#child_ions)
61    PL.reload_fly2('./ion.fly2', {init_ions=child_ions})
62    run()
63    spec:close()
64  end
```

Figure A.2.: Simion User Program Lines [32, 64]

In Fig. A.2 code lines 32 to 64 are shown. We are still in the "segment.flym" function. In this case I have scheduled and electron simulation followed by an ion simulation. Lines [17, 30] in Fig. A.1 set the electron simulation configuration. Lines [34, 63] sets the ion simulation configuration. Line 34 empties the "child_ions" array in case any ions from previous simulations are still contained in there. Lines [37, 50] are nearly identical to lines [17, 30] in Fig. A.1. The only differences are in the line 37 and 38. These electrons will now set ionization points along their trajectories during their simulation. Since ionization is evaluated at every time step of the simulation, there is a risk that one can create too many ions ($> 10^6$), which can overwhelm Simion leading to a crash. To stay on the secure side I reduce the electron amount from 10^5 in line 17 to 10^2 in line 37. The actual number of ions created is dependent on the ionization cross section given by Eq. 3. At lower potential settings for the EBIS the most ions are created, since the ionization cross section has its peak at around 80 eV electron kinetic energy. As a rule of thumb one can say a single electron produces about 1000-fold number of ions. A more detailed explanation of the ionization via virtual electron impact is given in Sec. 4.4. In line 38 the MCP potential is set negative for ion measurements. Lines [53, 63] prepare data recording, particle initialization, and runs the ion simulation. Lines [53, 55] creates the recording data file. Lines [56, 58] writes the data file header. In line 60 I make sure the variable "child_ions" exists and is an array. In line 61 "reload_fly2" is called, this time for the ions. The "ion.fly2" file is invoked and the "child_ions" array is passed on to "ion.fly2" for particle initialization. In line 62 the ion simulation is started and line 63 closes the recording file. Line 63 closes of the "segment.flym" function with the "end" command (not indented for better readability).

In Fig. A.3 code lines [65, 104] are shown. Lines [66, 67] is the "segment.initialize_run" function. This is the first function executed once when the "run" command is called (see line 62). Anything that needs to be done before the simulation is started can be done here. In lines [69, 85] the "segment.initialize" function is defined. This function is executed each time a particle is initialized for the simulation [27]. I use this function to record the initial conditions of the particles. In line 70 I use an if statement with the "last_write" variable declared on line 9, to check if this particular particle has already been recorded. Double recording occurs because the function is called once for every particle and for every potential instance type used in the simulation [28]. I use potential instances of electric and magnetic type. In lines [71, 74], I calculate the initial kinetic energy of electrons in atomic units. If ions are currently being simulated I instead calculate the initial kinetic energy of the argon in lines [75, 78]. Lines [80, 82] writes the initial conditions to the file. In line 84 "last_write" is set to the next particle number and line 85 closes off the "segment.initialize" function. In lines [87, 103] the "segment.fast_adjust" is define. This function is called at every time step in the trajectory simulation and is used to set the electric potentials of the electrodes.

```
65
66  function segment.initialize_run()
67  end
68
69  function segment.initialize()
70    if not (last_write == ion_number) then
71      if ion_charge == -1 then
72        m=1 --atomare einheiten
73        v_au=math.sqrt(ion_vx_mm^2 + ion_vy_mm^2 + ion_vz_mm^2)/convert_au_to_mmus
74        E_kin = m * v_au^2 /2 * 27.211  -- 1 E_hartree = 27.211 eV
75      elseif ion_charge == 1 then
76        m=1836.1526737600675 * 39.631 --Argon
77        v_au=math.sqrt(ion_vx_mm^2 + ion_vy_mm^2 + ion_vz_mm^2)/convert_au_to_mmus
78        E_kin = m * v_au^2 /2 * 27.211  -- 1 E_hartree = 27.211 eV
79      end
80      spec:write( ion_number, ',', ion_charge, ',', ion_time_of_flight, ',',
81                  ion_px_mm, ',', ion_py_mm, ',', ion_pz_mm, ',', ion_vx_mm, ',',
82                  ion_vy_mm, ',', ion_vz_mm, ',', E_kin, "\n")
83    end
84    last_write=ion_number
85  end
86
87  function segment.fast_adjust()
88      if ion_instance == 1 then
89          adj_elect03 = Vcat
90          adj_elect04 = V4
91          adj_elect05 = V5
92          adj_elect06 = V6
93          adj_elect07 = 0
94          adj_elect08 = Vrep
95          adj_elect09 = 0
96          adj_elect10 = 0
97      elseif ion_instance == 2 then
98          adj_elect11 = 0
99      elseif ion_instance == 3 then
100         adj_elect12 = 0
101         adj_elect13 = Vmcp
102     end
103 end
104
```

Figure A.3.: Simion User Program Lines [65, 104]

The object assembly of EBIS, vacuum chamber, MCP is divided into 3 instances in the simulation. This was done so I can maximize the number Simion grid cells in the EBIS instance at the cost of lower grid cells numbers for the other segments. In general, the more grid cells one uses in the simulation the more accurate the simulation will be. However, the total number of grid cells is limited by the computational resources available. For more details on grid cells I refer to previous works by the group [12]. Since I have 3 instances (not the same as instance types) the "fast_adjust" function has 3 "elseif" queries. Depending in which instance the simulated particle is currently in, the potentials in that instance have to be set. The individual electrodes are referenced with "adj_elect" followed by their specific number. The number they are assigned depends on the specifics of the electrode potential array conversion done in SL Tools [12].

```
105
106  -- Load field interpolation support.
107  local FieldArray = require "simionx.FieldArray"
108
109  -- Load solenoid field from data file.
110  local field = FieldArray("SimionReady_mike_bis_r=4_mitK.csv")
111
112
113  -- Override magnetic field in magnetic PA instances
114  -- with that in the field array.
115  function segment.mfield_adjust()
116    ion_bfieldx_gu, ion_bfieldy_gu, ion_bfieldz_gu =
117      field:get(ion_px_mm, ion_py_mm, ion_pz_mm)
118
119    ion_bfieldx_gu, ion_bfieldy_gu, ion_bfieldz_gu =
120        ion_bfieldx_gu*1e4, ion_bfieldy_gu*1e4, ion_bfieldz_gu*1e4
121
122  end
123
```

Figure A.4.: Simion User Program Lines [105, 123]

In Fig. A.4 code lines [105, 123] are shown. These are used in read in the magnetic field data and set the magnetic field in the simulation. Line 107 loads the support module for defining field array. In line 110 the magnetic field data is read-in. In lines [115, 122] the "segment.mfield_adjust" is defined. This function is the magnetic analogue to the "fast_adjust" function for electric fields. In lines [116, 117] the magnetic field is set. In lines[119, 120] the magnetic field is converted from Tesla to Gauss units, required by Simion. Line 122 closes the "segment.mfield_adjust" function. More details on the

magnetic field data implementation is given in Sec. 4.2.

```
124  -------IONISATION------------
125
126  --Thermal impulse distribtion--
127  local convert_au_to_mmus = 2187.691264 -- 1 a0*E_hartree/a0 = hbar/a0/m_electron
128  local m_ion = 1836.1526737600675 * 39.631 --Argon
129  local k=1.380649e-23 / (4.3597447222071e-18)
130  local A=4*math.pi/m_ion*(m_ion/2/math.pi/k/T)^(3/2) * (1/m_ion)^2
131  local B=1/2/m_ion/k/T
132  local function mb(p)
133    return A * p^2 * math.exp(-B * p^2)
134  end
135
136  local function mb_v(evx, evy, evz)
137    p_MB=math.random()*4*math.sqrt(1/B)
138      while not (mb(p_MB)>(math.random()*mb(math.sqrt(1/B)))) do
139      p_MB=math.random()*4*math.sqrt(1/B)
140      end
141
142    theta = math.acos(evx/math.sqrt(evx^2 + evy^2 + evz^2))
143    alpha = (2*math.random()-1)*math.pi/2
144    while not (math.cos(alpha)^2 > math.random()) do
145      alpha = (2*math.random()-1)*math.pi/2
146    end
147
148      theta = theta + math.pi/2 + alpha     -- in rad
149      phi = 2*math.pi*math.random()       -- in rad
150      pzMB = p_MB*math.sin(theta)*math.cos(phi)   -- in a.u.
151      pyMB = p_MB*math.sin(theta)*math.sin(phi)   -- in a.u.
152      pxMB = p_MB*math.cos(theta)       -- in a.u.
153      vx = (pxMB/m_ion)*convert_au_to_mmus    --p and ion mass in a.u. -> in mm/us
154      vy = (pyMB/m_ion)*convert_au_to_mmus    --p and ion mass in a.u. -> in mm/us
155      vz = (pzMB/m_ion)*convert_au_to_mmus    --p and ion mass in a.u. -> in mm/us
156    v={vx,vy,vz}
157    return v
158  end
159
```

Figure A.5.: Simion User Program Lines [124, 159]

In Fig. A.5 code lines [124, 159] are shown. In these lines the ionized argon is given its initial kinetic energy and momentum direction. In line 127 the conversion variable

is stated again. This step is not necessary since the variable in already defined in line 3. I define it here again for visibility because it will be frequently needed in the following lines. In line [128, 129] the argon mass and the Boltzmann's constant are defined in atomic units. In line 130 the factor of the normalized Maxwell-Boltzmann velocity distribution is defined. In line 131 the factor in the exponent of the distribution is calculated. Lines [132, 134] a function is defined which returns the probability of a specific momentum value given by the normalized Maxwell-Boltzmann velocity distribution. In lines [136, 158] a function is defined which returns the velocity vector for the argon ion

```
160  --Cross section (PetersonAllen1972)--
161  local I = 15.76
162  local E_CSmax = 74.1559846658151 --WolframAlpha in eV
163  local function CS(E) -- E muss in eV sein
164    local c = 10.3
165    local D = (13.2/E) * math.log((E + (120/E))/I)
166    local T_0 = 2 - (100/(E+10))
167    return D * -1 * c * (math.atan((T_0 - (E-I)/2)/c) - math.atan(T_0/c))
168  end
169
170  --List of Ions--
171  local function add_ion(t)
172    local particle = {}
173    particle.tob = t.tob or ion_time_of_birth
174    particle.tof = t.tof or ion_time_of_flight
175    particle.mass = t.mass or 39.631 --Argon
176    particle.charge = t.charge or 1
177    particle.px = t.px or ion_px_mm
178    particle.py = t.py or ion_py_mm
179    particle.pz = t.pz or ion_pz_mm
180
181    particle.vx = t.vx
182    particle.vy = t.vy
183    particle.vz = t.vz
184    particle.color = t.color or 3
185
186    child_ions[#child_ions+1] = particle  -- append
187
188    return particle
189  end
190
```

Figure A.6.: Simion User Program Lines [160, 190]

dependent on the velocity direction of the electron that ionized it. We give the ion a kinetic energy via the Maxwell-Boltzmann velocity distribution. However, this velocity is not applied isotropically. Instead we use McConkey et al [22] directional momentum distribution. In lines [137, 140] a momentum value for the ion is diced via Maxwell-Boltzmann velocity distribution. In lines [142, 146] the momentum direction of the ion is calculated. In line 142 I calculate the polar angle between the electron velocity vector to the beam axis direction $\vec{e}_x$. In lines [143, 146] a $\cos^2(\alpha)$ distributed random angle within a $[-\frac{\pi}{2}, \frac{\pi}{2}]$ range is selected. In line 148 "theta" is redefined to be the polar angle of the ion velocity vector. In line 149 a random azimuth angle is selected. In lines [150, 152] the momentum vector components are converted from polar coordinates to Cartesian coordinates. In lines [153, 155] the velocity components are converted from atomic unit to Simion units. In lines [156, 157] in a velocity array is created, set, and returned.

In Fig. A.6 code lines [160, 190] are shown. In lines [161, 168] the cross section Eq. 4 is written. In line 161 the first ionization energy for argon is given and in line 162 the kinetic energy is written which gives the maximum of the electron impact ionization cross section for argon. Lines [163, 168] define a function which takes the kinetic energy of the projectile electron and returns the corresponding ionization cross section. Lines [171, 189] define a function which takes a particles properties and inserts them in the array "child_ions". The array "child_ions" is used to initialize the ions for simulation after the electron simulation has conducted.

In Fig. A.7 code lines [191, 215] are shown. These lines define the function "segment.other_actions". This function is executed at every time step of a simulation. The virtual electron impact ionization is implemented in this function. In lines [194, 198] I calculate the kinetic energy of the currently simulated electron. If an ion is currently simulated this "elseif" query is skipped. Lines [200, 207] implement the virtual electron impact ionization. In the "elseif" query I use "ion_color" and "ion_charge" as conditions to make sure an electron is currently simulated which can "ionize" an argon atom. The next conditional selects a random value between 0 and the cross section maxima and compares it to the cross section value calculated from the current electron kinetic energy. If this condition is fulfilled virtual ionization may occur. The next condition checks if the MCP potential is negative, since I only want to simulate ions when the MCP is set to a negative potential. The last condition makes sure ionization only occurs on negative potential slopes. These are the only ions that may reach the MCP since they are accelerated forwards towards the exit of the EBIS. Ions created on positive slopes are accelerated backwards and therefore cannot reach the MCP. If all these conditions are fulfilled an ion is created. Line 204 places a mark in the electron trajectory where ionization has occurred. Line 205 calls the "mb_v" function, defined in lines [136, 158],

```
191  -- Called on every time-step.
192  function segment.other_actions()
193
194    if ion_charge==-1 then
195      m_e=1 --atomare einheiten
196      v_au = math.sqrt(ion_vx_mm^2 + ion_vy_mm^2 + ion_vz_mm^2)/convert_au_to_mmus
197      E_kin = m_e * v_au^2 /2 * 27.211  -- 1 E_hartree = 27.211 eV
198    end
199
200    if (ion_color == 1 and ion_charge==-1 and
201        ((CS(E_CSmax)*math.random()) < CS(E_kin)) and
202        Vmcp<0 and ion_dvoltsx_mm<0) then
203
204      mark()
205      v=mb_v(ion_vx_mm, ion_vy_mm, ion_vz_mm)
206      add_ion{mass = 39.631, charge = 1, vx=v[1], vy=v[2], vz=v[3], color=3}
207    end
208
209    --stop ions from endlessly oscillating around repeller
210    if (ion_charge==1 and ion_px_mm > 60 and ion_vx_mm < 0) or
211       (ion_time_of_flight > 1e4) then
212      ion_splat=1
213    end
214  end
215
```

Figure A.7.: Simion User Program Lines [191, 215]

and return the initial velocity vector for the ion. Line 206 adds the ion to the array "child_ion". Lines [210, 213] stop ion simulations that do not or take too long to reach the MCP.

In Fig. A.8 code lines [216, 240] are shown. In lines [217, 235] defines the "segment.terminate" function. This function is called every time a simulation of a particle has concluded. The code are identical to lines [69, 85] where "segment.initialize" is defined. The "segment.terminate" is used to record the final conditions of the particles. Line 218 checks if the particle has already been recorded. Lines [219, 222] calculates the final kinetic energy of the particle if the last particle simulated was an electron. Lines [223, 226] calculates the final kinetic energy of the particle if it was an argon ion. Lines [229, 231] write the final conditions into the data file. In line 234 the variable "last_write" is updated and line 235 closes the "segment.terminate" function. Lines [237, 238] feature the "segment.terminate_run()" function. This function is executed each time a full simulation run has concluded. This function can be used to do anything after the simulation run.

```
216
217 function segment.terminate()
218   if not (last_write == ion_number) then
219     if ion_charge == -1 then
220       m=1 --atomare einheiten
221       v_au=math.sqrt(ion_vx_mm^2 + ion_vy_mm^2 + ion_vz_mm^2)/convert_au_to_mmus
222       E_kin = m * v_au^2 /2 * 27.211  -- 1 E_hartree = 27.211 eV
223     elseif ion_charge == 1 then
224       m=1836.1526737600675 * 39.631 --Argon
225       v_au=math.sqrt(ion_vx_mm^2 + ion_vy_mm^2 + ion_vz_mm^2)/convert_au_to_mmus
226       E_kin = m * v_au^2 /2 * 27.211  -- 1 E_hartree = 27.211 eV
227   end
228
229     spec:write(ion_number, ',', ion_charge, ',', ion_time_of_flight, ',',
230                ion_px_mm, ',', ion_py_mm, ',', ion_pz_mm, ',', ion_vx_mm, ',',
231                ion_vy_mm, ',', ion_vz_mm, ',', E_kin, "\n")
232   end
233
234   last_write=ion_number
235 end
236
237 function segment.terminate_run()
238 end
239
240
```

Figure A.8.: Simion User Program Lines [216, 240]